Title: Tyrosinase-induced neuromelanin accumulation triggers rapid dysregulation and degeneration of the mouse locus coeruleus

Abbreviated Title: Neuromelanin damages the locus coeruleus

Alexa F. Iannitelli[1*], Leslie Hassanein[1*], Margaret M. Tish[1], Bernard Mulvey[2,3,4], Harris E. Blankenship[5], Anu Korukonda[1], L. Cameron Liles[1], Amanda L. Sharpe[6], Jean-Francoise Pare[7,8], Rosa Villalba[7,8], Arielle Segal[1], Steven A. Sloan[1], Keri Martinowich[3,4], Joseph D. Dougherty[2], Katharine E. McCann[1], Yoland Smith[7,8], Michael J. Beckstead[5], David Weinshenker[1#]

[*]Equal contributions

[1]Department of Human Genetics, Emory University School of Medicine, Atlanta, GA 30322, USA

[2]Department of Psychiatry, Intellectual and Developmental Disabilities Research Center, Washington University School of Medicine, St. Louis, MO 63110, USA

[3]Lieber Institute for Brain Development, Johns Hopkins Medical Campus, Baltimore, MD, 21205, USA.

[4]Department of Psychiatry and Behavioral Sciences, Johns Hopkins School of Medicine, Baltimore, MD, 21205, USA.[2]Department of Genetics, Washington University School of Medicine, St. Louis, MO 63110, USA

[5]Aging & Metabolism Research Program, Oklahoma Medical Research Foundation, Oklahoma City, OK 73104

[6]Department of Pharmaceutical Sciences, University of Oklahoma Health Sciences Center, Oklahoma City, 73117

[7]Department of Neurology, Emory University School of Medicine, Atlanta, GA 30322, USA

[8]Emory National Primate Research Center, Emory University, Atlanta, GA 30329, USA

[#]Address correspondence to:

David Weinshenker, PhD

Department of Human Genetics

Emory University School of Medicine

615 Michael St., Whitehead 301

Phone: (404) 727-3106

Email: dweinsh@emory.edu

Abstract

The locus coeruleus (LC), the major source of norepinephrine (NE) in the brain, is among the earliest site of pathology in both Alzheimer's disease (AD) and Parkinson's disease (PD), and it undergoes catastrophic degeneration later in both disorders. Dysregulation of the LC is thought to contribute to prodromal symptoms of AD and PD such as anxiety and sleep disturbances, while frank LC loss promotes cognitive decline. However, the mechanisms responsible for its selective vulnerability are unknown. It has been suggested that neuromelanin (NM) pigment contributes to LC susceptibility, but causal relationships have been difficult to test because rodents do not naturally produce NM. Here, we report that viral-mediated expression of human tyrosinase induced pigmentation in mouse LC neurons that recapitulated key features of natural primate NM. One week of NM accumulation resulted in LC neuron hyperactivity, reduced tissue NE levels, transcriptional changes, and anxiety-like behavior. By 6-10 weeks, NM accumulation was associated with severe LC neuron neurodegeneration and microglial engulfment of the pigment granules, while the anxiety-like behavior abated. These phenotypes are reminiscent of LC dysfunction and cell death in AD and PD, validating this model for studying the consequences of NM accumulation in the LC as it relates to neurodegenerative disease.

Significance Statement

Alzheimer's disease (AD) and Parkinson's disease (PD) are two of the most common neurodegenerative diseases worldwide. Because therapies that cure or even prevent their progression are lacking, research is focused on the identifying earliest signs of disease as targets for diagnosis and treatment. The locus coeruleus (LC), the main source of the neurotransmitter n norepinephrine (NE) in the brain, is one of the first brain regions affected in both AD and PD. LC dysregulation promotes prodromal AD and PD symptoms, while its degeneration accelerates disease progression. Here we identify neuromelanin (NM) pigment as a LC vulnerability factor that induces neuronal hyperactivity followed by cell death. Approaches that mitigate NM accumulation and toxicity may target the earliest phases of neurodegenerative disease.

Introduction

The neurodegenerative diseases Alzheimer's disease (AD) and Parkinson's disease (PD) are among the most common causes of dementia and movement disorders, respectively. The noradrenergic locus coeruleus (LC), the major source of central norepinephrine (NE) is one of the earliest brain regions to accumulate tau pathology in AD and α-synuclein pathology in PD (Braak et al., 2001; Del Tredici et al., 2002; Braak and Del Tredici, 2011b, a; Braak et al., 2011; Pletnikova et al., 2018; Gilvesy et al., 2022; Bueicheku et al., 2024), and it undergoes catastrophic degeneration later in both diseases (Mann et al., 1980; Bondareff et al., 1982; Iversen et al., 1983; Mann and Yates, 1983a; German et al., 1992; Zarow et al., 2003; Theofilas et al., 2017). Both clinical and animal model research has identified early LC-NE dysfunction as a trigger for prodromal symptoms in AD and PD typified by sleep abnormalities and neuropsychiatric symptoms such as anxiety, depression, and apathy (Remy et al., 2005; Prediger et al., 2012; Ehrenberg et al., 2017; Ehrenberg et al., 2018; Sommerauer et al., 2018; Weinshenker, 2018; Butkovich et al., 2020; Gilvesy et al., 2022; Kelberman et al., 2022; Ye et al., 2022; Iannitelli et al., 2023b; Falgas et al., 2024), while subsequent frank LC degeneration predicts and exacerbates cognitive decline (Zweig et al., 1993; Heneka et al., 2006; Vazey and Aston-Jones, 2012; Rorabaugh et al., 2017; Chalermpalanupap et al., 2018; Weinshenker, 2018; Ghosh et al., 2019; Li et al., 2019; Jacobs et al., 2021; Prokopiou et al., 2022; Ye et al., 2022; Bueicheku et al., 2024).

The specific factors that make LC neurons vulnerable to pathology, dysfunction, and death in AD and PD are not fully understood, although several potential contributors have been identified including pacemaker activity, toxic NE metabolites, thin unmyelinated axons, and neuromelanin (NM) (Weinshenker, 2018; Kang et al., 2020; Matchett et al., 2021; Kang et al., 2022; Iannitelli et al., 2023a; Iannitelli and Weinshenker, 2023).

NM is a dark pigment found exclusively in catecholaminergic cells of the LC and substantia nigra pars compacts (SNc), which are also vulnerable in PD (Zecca et al., 2004; Zecca et al., 2008b). NM is a byproduct of catecholamine synthesis and metabolism, and the formation of NM likely results from an overabundance of catecholamines that cannot be sequestered into vesicles quickly enough in active neurons (Sulzer et al., 2000). In addition to catecholamine metabolites, these granules contain melanins (Bush et al., 2006), lipid droplets, protein aggregates (Sulzer et al., 2008), and heavy metals (Zecca et al., 2008b). Thus, it has been proposed that the primary function of NM is to bind and sequester these harmful compounds in the cytoplasm so that they do not harm the neurons (Zecca et al., 2003). However, the buildup of NM may exacerbate neurodegeneration in AD and PD either by interfering with cellular machinery and/or via release of previously bound toxins as it breaks down during cell death. Indeed, LC neurons containing the highest amounts of NM are disproportionately lost during both normal aging and PD (Mann and Yates, 1983b).

Establishing a causal relationship between NM and LC degeneration has been difficult because NM is not produced endogenously in rodents (Barden and Levine, 1983), which comprise the majority of animal models for studying AD and PD. A breakthrough came when researchers were able to drive NM formation in the SNc of mice and rats through viral-mediated expression of human tyrosinase (hTyr), the biosynthetic enzyme responsible for melanin production in the skin (Carballo-Carbajal et al., 2019). In this model, NM expression in the SNc resulted in neurodegeneration and subsequent motor impairments similar to those seen in other mouse models of PD. We adapted this strategy to promote NM accumulation in the mouse LC to gain insight into the molecular mechanisms of NM-mediated adaptations and neurotoxicity in a region of selective early vulnerability in AD and PD.

Materials and Methods

Animals. Adult male and female mice were used for all behavioral and immunohistochemical experiments. For immunohistochemistry, behavior, and HPLC, TH-Cre mice (B6.Cg-7630403G23RikTg(Th-cre)1Tmd/J, The Jackson Laboratory, # 008601) were used for the specific expression of Cre-dependent viral vectors in the LC. For translating ribosome affinity purification (TRAP) RNA-sequencing experiments, we crossed TH-Cre mice with transgenic *Slc6a2-eGFP/Rpl10a* mice (B6;FVB-Tg(*Slc6a2-eGFP/Rpl10a*)JD1538Htz/J, The Jackson Laboratory, #031151), which incorporate an EGFP/Rpl10a ribosomal fusion protein into a bacterial artificial chromosome under the *Slc6a2* (NE transporter; NET) promoter to allow for the isolation of polysomes and translating mRNAs specifically from noradrenergic neurons (Mulvey et al., 2018). Mice were group housed with sex- and age-matched conspecifics (maximum of 5 animals per cage) until one week prior to behavioral testing, and then individually housed for the subsequent week of experimentation until sacrifice. Animals were maintained on a 12:12 light:dark cycle (lights on at 0700), and food and water were available *ad libitum*, unless otherwise specified. All experiments were conducted at Emory University in accordance with the National Institutes of Health *Guideline for the Care and Use of Laboratory Animals* and approved by the Emory Institutional Animal Care and Use Committee.

Viral vectors. To express hTyr in the LC, we developed an AAV5-EF1a-DIO-hTyr construct with assistance from the Emory Custom Cloning and Viral Vector Cores. For some preliminary experiments (immunohistochemistry for viral confirmation and gliosis, stereology), all mice were injected with AAV5-DIO-hTyr, and TH-Cre+ animals were used as the experimental group while TH-Cre- littermates served as the controls. For the remaining experiments, only TH-Cre+ mice

were used, and mice were injected with either the AAV5-DIO-hTyr experimental virus or a comparable AAV5-DIO-EYFP control virus (Addgene, plasmid #27056).

Stereotaxic injections. Stereotaxic infusions were be performed as previously described (Tillage et al., 2020a), in a stereotaxic frame under 2.0% isoflurane anesthesia. Bilateral LC infusions were made at a volume of 0.5 µL/hemisphere using a 5 µL Hamilton glass syringe. The virus was infused at a rate of 0.15 µL/min, and the needle was allowed to remain in place for 5 min following the completion of each infusion. LC coordinates are AP: - 5.4mm, ML: +/- 1.2mm, and DV: -4.0mm relative to Bregma.

High Performance Liquid Chromatography (HPLC). Mice were anesthetized with isoflurane and euthanized by rapid decapitation. The pons, prefrontal cortex, and hippocampus were rapidly dissected on ice and flash-frozen in isopentane (2-Methylbutane) on dry ice. The samples were weighed and stored at -80°C until processing for HPLC by the Emory HPLC Bioanalytical Core. As previously described (Lustberg et al., 2022), tissue was thawed on ice and sonicated in 0.1 N perchloric acid (10 µl/mg tissue) for 12 s with 0.5 s pulses. Sonicated samples were centrifuged (16,100 rcf) for 30 min at 4 °C, and the supernatant was then centrifuged through 0.45 µm filters at 4000 rcf for 10 min at 4 °C. For HPLC, an ESA 5600A CoulArray detection system, equipped with an ESA Model 584 pump and an ESA 542 refrigerated autosampler was used. Separations were performed using an MD-150 × 3.2 mm C18, 3 µm column (Thermo Scientific) at 30 °C. The mobile phase consisted of 8% acetonitrile, 75 mM NaH2PO4, 1.7 mM 1-octanesulfonic acid sodium and 0.025% trimethylamine at pH 2.9. A 20 µL of sample was injected. The samples were eluted isocratically at 0.4 mL/min and detected using a 6210 electrochemical cell (ESA, Bedford,

MA) equipped with 5020 guard cell. Guard cell potential was set at 475 mV, while analytical cell potentials were −175, 100, 350 and 425 mV. The analytes were identified by the matching criteria of retention time measures to known standards (Sigma Chemical Co., St. Louis MO). Compounds were quantified by comparing peak areas to those of standards on the dominant sensor.

Immunohistochemistry. Mice were euthanized with an overdose of sodium pentobarbital (Fatal Plus, 150 mg/kg, i.p.; Med-Vet International, Mettawa, IL) and were transcardially perfused with cold 4% PFA in 0.01 M PBS for light microscopy and 4% PFA + 0.1% glutaraldehyde for electron microscopy. After extraction, brains were post-fixed overnight in 4% PFA at 4°C and then transferred to a 30% sucrose/PBS solution for 72 h at 4°C. Brains were embedded in OCT medium (Tissue-Tek) and sectioned by cryostat into 40-um-thick coronal sections at the level of the LC, anterior cingulate cortex (ACC), and hippocampus. Sections were blocked in 5% normal goat serum (NGS) in 0.01 M PBS/0.1% Triton-X permeabilization buffer and then incubated for 24 h at 4°C in NGS blocking buffer with primary antibodies listed in **Table 1**. Following washes in 0.01 M PBS, sections were incubated for 2 h in blocking buffer including secondary antibodies listed in **Table 1**. After washing, sections were mounted onto Superfrost Plus slides and cover-slipped with Fluoromount-G plus DAPI (Southern Biotech, Birmingham, AL).

Fluorescence Microscopy. For the catecholaminergic marker tyrosine hydroxylase (TH) and hTyr, immunofluorescent micrographs were acquired on a Leica DM6000B epifluorescent upright microscope at 20x magnification with uniform exposure parameters for each stain and region imaged. Brightfield images of pigment granules were also obtained on the Leica DM6000B upright microscope at 20x magnification. Following convention, these images are oriented with the dorsal

direction up and the ventral direction down. For astrocyte marker glial fibrillary acidic protein (GFAP) and LC terminal marker NE transporter (NET), listed in **Table 1**, immunofluorescent images were acquired as z-stack images (10 z-stacks; pitch: 0.1 µm) at 20x magnification and compressed on a Keyence BZ-X700 microscope system. One representative atlas-matched section was selected from each animal. Image processing for all images was conducted using the FIJI/ImageJ software.

Electron microscopy.

Tissue collection and processing. All brains prepared for electron microscopy, perfused with a Ringer's solution and a mixture of paraformaldehyde (4%) and glutaraldehyde (0.1%), were cut in 60 µm-thick coronal sections with a vibrating microtome. Selected sections that included the LC were immunostained with specific antibodies against TH (dilution 1:2000; Millipore, AB152; RRID: AB_390204), IBA-1 (dilution 1:500; Abcam; Ab5076; RRID: AB_2224402) and GFAP (dilution 1:5000; Abcam AB7260; RRID: RRID:AB_305808) according to the avidin biotin complex method (ABC-Vectastain Standard kit, Vector Labs), using DAB as chromogen for the peroxidase reaction. Following the DAB reaction, sections were transferred to a phosphate buffer solution (PB, 0.1 M, pH 7.4).

Transmission electron microscopy (TEM). The tissue processed for TEM was postfixed in a 1% osmium tetroxide solution for 20 min. Following washes in PB, and then the samples were dehydrated in alcohol solutions (50–100%) before being placed in propylene oxide. Uranyl acetate (1%) was added to the 70% alcohol to increase contrast in the electron microscope. The dehydrated sections were embedded in epoxy resin (Durcupan, ACM; Fluka, Buchs, Switzerland) for 12 h, mounted onto oil-coated slides and cover-slipped before being baked at 60ºC for 48 h. Blocks of

LC tissue were then taken out from the slide, glued on resin blocks and cut in ultrathin sections (70 nm-thickness) using an ultramicrotome (Ultra-cut T2; Leica, Germany) and mounted onto single slot Pioloform-coated copper grids. Grids were then examined with an electron microscope (EM; Jeol; Model 1011) coupled with a CCD camera (Gatan; Model 785) controlled with DigitalMicrograph software (Gatan; version 3.11.1).

For ultrastructual comparisons of hTyr-induced NM in mice and naturally produced NM in primates, three brainstem sections at the level of LC from a 16-year-old rhesus macaque were processed according to the same procedure and examined in the electron microscope.

Serial Block Face/Scanning Electron Microscope (SBF/SEM) and 3D ultrastructural reconstruction. Samples of GFAP- and IBA-1-immunostained tissue were sent to the Oregon Health Science University Microscopy Core for serial sectioning/imaging using an SBF/SEM, which allows for the collection of serial digitized electron microscopic images (about 100-200 images/stack). The images (TIFF format) were imported into the *Reconstruct* (NIH) software (https://synapseweb.clm.utexas.edu/software-0), the section thickness (65-70nm) and the pixel size (0.0045µm) were adjusted before the segmentation, and the contours of the different elements analyzed were manually traced with different color code lines in each serial electron micrograph.

Cell counts. Mice (n=3) were given a unilateral infusion of AAV5-DIO-hTyr virus targeting the LC. The contralateral LC was infused with AAV5-DIO-EYFP. One week later, animals were perfused as described above. Brains were sectioned at 40um on a cryostat, and sections were processed for immunohistochemistry to stain for TH and NISSL. Images were taken at 4x and 20x on a Keyence BZ-X800 microscope. A z-stack (2um pitch, 20 images total) was acquired for all 20x images and the full focus image was used for analysis. Brightfield images to capture NM expression were transformed into fluorescence images using HALO v3.6 Deconvolution (Indica

Labs) and fused with fluorescence images of TH and NISSL. Cell counts were quantified using HALO v3.6 FISH-IF v2.1.4 software. Cells were defined using either NISSL or TH and then counted within the region of interest delineating the LC. LC borders were defined using TH and NM. Me5 cells, which fluoresce brightly in all channels and are much larger and rounder than LC cells, were excluded from the boundaries of analysis. Parameters used to define cells were set for each animal and used consistently across all sections for that animal.

Translating Ribosome Affinity Purification (TRAP). To obtain adequate quantities of RNA for sequencing, samples from two 6-8 month-old, same-sex and treatment TH-Cre+, *Slc6a2-eGFP*/*Rpl10a*+ mice were pooled to form a biological replicate by dissecting out the hindbrain posterior to the pontine/hypothalamic junction (cerebellum was discarded). Six biological replicates were collected per treatment group. Each replicate was homogenized and TRAP was performed as described (Mulvey et al., 2018; Iannitelli et al., 2022), resulting in LC-enriched "TRAP" samples and whole-hindbrain "input" samples. RNA was extracted using Zymo RNA Clean & Concentrator-5 kit, and subsequently sent for polyA-enriched library preparation and Illumina sequencing by NovoGene to a minimum depth of 20 million fragments per sample. Forward and reverse sequencing files from each replicate were aligned to the mouse genome (mm10) using STAR alignment, and counts were obtained using FeatureCounts in R Bioconductor. Two samples from saline-treated mice were removed from analysis because the TRAP protocol failed to enrich *Slc6a2* above a 10-fold change, a quality control threshold observed in all other saline-treated samples. Sequencing data are available on NCBI GEO (GSE226827).

DE analysis. Gene counts data were imported into R 4.4.1 on a Macintosh for analysis using *edgeR* and the *voomWithQualityWeights* (Mulvey et al., 2023) implementation as

incorporated into *voomLmFit*. Counts data were imported and distributions of counts visualized to determine a low-count cutoff, which we set to 70, requiring at least 5 samples to exceed this threshold for a given gene. 13,213 genes were therefore retained for downstream differential expression analyses. TMM normalization factors were then calculated to account for sequencing library size (Mulvey et al., 2023). DE analysis was performed using a model covering 4 groups: EYFP input, EYFP TRAP (LC), hTyr input, and hTyr TRAP, allowing us to compare both TRAP vs. input (within condition) TRAP vs. TRAP (across conditions) using the same fitted data. Our model was set up as *~0+group* and initialized in *voomLmFit* with sample weights enabled (as is implicit in the predecessor, *voomWithQualityWeights*). *voomLmFit* acts as a wrapper around multiple DE pipeline steps in that it executes *duplicateCorrelation* (Smyth et al., 2005) at the level of replicate to correct for multiple samples having been collected from the same mice (every given homogenate was split into an input and a TRAP fraction), and further executes *voomWithQualityWeights* a second time to refine parameter estimates and *lmFit* to fit the model. We subsequently used *topTable* to collect full DE stats for each of the four comparisons of interest.

Gene Set Enrichment Analysis (GSEA). To test for enrichment of DE genes in ontology and literature-derived sets, we utilized the threshold-free GSEA method (Subramanian et al., 2005) and its accompanying gene set catalogs (curated/C2, regulatory targets/C3, ontologies/C5, oncogenic/C6, and cell type signatures/C8) in mSigDB version 2024.1 mouse, implemented using the R package *fGSEA* (Korotkevich et al., 2021). We additionally collated several additional TF-target gene sets to test for enrichment: ChEA 2022 resource (Keenan et al., 2019), TRRUST (Han et al., 2018), those mined from publication supplements in Rummagene (Clarke et al., 2024), and as curated in the Enrichr (Xie et al., 2021) package (Gene Expression Omnibus-mined results of TF perturbation experiments and TF protein-protein interactions). We input the signed DE *t*

statistics for use as the DE gene ranking values to *fGSEA* with analysis parameters as follows: gene set sizes 15-500; *eps* (specifying range over which to calculate p-values) set to 0 to return a p-value for all tests; and 50,000 permutations for initial p-value estimations. For mSigDB sets, *fGSEA*'s *collapsePathways* function was then used to consolidate results to represent the strongest/most specific enrichments from overlapping sets (in other words, the most granular set based on *de novo* calculation of a hierarchy of sets).

For analysis of DEG data reported in (Mathys et al., 2019), we utilized the provided DE analysis results from Supplemental Table 2 for excitatory neurons, with the signed 'MixedModel.z' statistic used as the DE ranking variable. We utilized the same collated TF-target gene sets as used for GSEA analysis of our data. fGSEA parameters were gene set sizes 15-500; *eps* set to 0 to return a p-value for all tests; and 10,000 permutations for initial p-value estimations. While we performed analyses using the full corpus of TF-target sets to ensure comparable multiple testing correction, we only examined TF-target sets corresponding to *ATF6* and *XBP1* for interpretation of this analysis.

STRING Protein-Protein Interactors for Xbp1 and Atf6. To determine physical interactors of *Xbp1* and *Atf6*, we queried mouse protein-protein interactions indexed in STRINGdb v12.0 by searching the two mouse gene symbols. Subsequently, we filtered to interactions listed as "high confidence (>0.7)" and downloaded the list of 82 mouse protein interactors meeting this criterion, 55 of which were included in the DE analysis. We then examined the hTyr-LC vs. EYFP-LC DE table for significant DEGs among these interactors. The result of this STRINGdb query is included in **Supplemental Tab Yn**.

Electrophysiology. Mice were deeply anesthetized with isoflurane and decapitated. Brains were rapidly removed and sectioned in ice-cold cutting solution containing (in mM): 110 choline

chloride, 2.5 KCl, 1.25 Na_2PO_4, 0.5 $CaCl_2$, 10 $MgSO_4$, 25 glucose, 11.6 Na-ascorbate, 3.1 Na-pyruvate, 26 $NaHCO_3$, 12 N-acetyl-L-cysteine, and 2 kynurenic acid. Horizontal (220 µm) slices containing the LC at the level of the mesencephalic trigeminal tract neurons (ME5) were collected and transferred to a holding chamber containing artificial cerebrospinal fluid (aCSF) containing (in mM) 126 NaCl, 2.5 KCl, 1.2 $MgCl_2$, 2.4 $CaCl_2$, 1.2 NaH_2PO_4, 21.4 $NaHCO_3$, and 11.1 glucose plus 1 Na ascorbate, 1 Na pyruvate, 6 N-acetyl-L-cysteine and MK-801 to minimize excitonic effects induced by sectioning. Slices recovered for 30 min at 32°C followed by at least 30 min at room temperature prior to recording.

Slices were transferred to a recording chamber where they were perfused with warmed aCSF (inline heater, 32-34°C, Warner Instruments) at a rate of approximately 2 mL/min via gravity or a peristaltic pump (Warner Instruments). Slices were visualized under Dödt gradient contrast (DGC) optics on an upright microscope (Nikon FN1 or Zeiss Examiner D1). Putative LC-NE neurons were identified first by location (immediately medial to ME5 neurons, rostral to the fourth ventricle) and large (>20 µm) cell bodies, followed by visual presence of NM or EYFP fluorescence (controls). Electrophysiological parameters for LC-NE neuron identification included slow, irregular spontaneous action potential generation, presence of A-type potassium currents and a rebound delay after a hyperpolarizing step (-100 pA) in current clamp and low input resistance (approximately 100 MΩ, -60 V_{hold}) (Williams et al., 1984). Thin wall glass (World Precision Instruments or Warner Instruments) was used for cell-attached and whole-cell recordings, patch pipettes were pulled from thin-wall glass, and displayed resistances of 2.5-3 MΩ when filled with an intracellular solution containing (in mM): 135 K gluconate, 10 HEPES, 5 KCl, 5 $MgCl_2$, 0.1 EGTA, 0.075 $CaCl_2$, 2 ATP, 0.4 GTP, pH 7.35, liquid junction potential was calculated to be -17 mV, and was not corrected. Cell attached recordings were conducted

using a Na-HEPES based intracellular solution (plus 20 mM NaCl, 290 mOsm/L, pH 7.4) (Branch and Beckstead, 2012). Frequency-current (F-I) relationships were calculated as spikes per second across the 2 second depolarization step. Gain was calculated as the slope of the steady state F-I curve, from 0-250pA. Cell-attached frequency was calculated as spikes per second during a 30 second sweep.

Behavioral assays. Behavioral assays were performed in the following order, from least to most stressful.

Sleep latency: Latency to sleep was measured as the duration of time it took for the mouse to fall asleep following mild stimulation (gentle handling). A sleep bout was defined as 2 min of uninterrupted sleep behavior, followed by 75% of the following 8 min (Hunsley and Palmiter, 2004). This assay has been previously validated using EEG recordings (Porter-Stransky et al., 2019). Sleep testing began at 9:00 A.M., 2 h into the light cycle when mice typically engage in sleep behavior naturally. Videos were recorded for each session and scored by an experienced observer. Previous research by our group and other has revealed that increasing LC-NE transmission decreases sleep latency, while NE depletion has the opposite effect (Porter-Stransky et al., 2019).

Novelty-suppressed feeding: Chow was removed from individual home cages 24 h prior to behavioral testing. Mice were moved to the test room under red light and allowed to habituate for 2 h prior to the start of the test. Individual mice were placed in a novel arena (10” × 18” × 10”) with a single pellet of standard mouse chow located in the center. The latency to feed, operationally defined as grasping and biting the food pellet, was recorded using a stopwatch. Mice that did not feed within the 15-min period were assigned a latency score of 900 s (Tillage et al., 2020b). We

have shown that increasing NE promotes anxiety-like behavior in this task reflected by longer latencies to eat in the novel environment, while decreasing attenuates anxiety and reduces latency to eat (Lustberg et al., 2020).

Fear conditioning and context testing: Fear-conditioning training and subsequent contextual fear testing is a widely used assessment of associative memory, particularly for an environment in which an aversive stimulus (footshock) was previously administered. This method has been described previously by our group and others and is sensitive to changes in NE (Murchison et al., 2004; Chalermpalanupap et al., 2018; Butkovich et al., 2020). Mice were placed in a fear-conditioning apparatus (7 in. x 7 in. x 12 in.; Coulbourn Instruments) with a metal shock grid floor. Following 3 min of habituation, three conditioned stimulus (CS)-unconditioned stimulus (US) pairings were presented with a 1-minute intertrial interval. The CS was a 20-second, 85 dB tone which co-terminated with the US, a 2-s, 0.5 mA footshock (Precision Animal Shocker, Colbour Instruments). The following day, the context test was conducted by placing animals back into the fear conditioning chamber without the administration of CS-US pairings. Freezing behavior was measured as a readout of memory for the fear-associated context.

Statistical analyses. Cell counting and HPLC measurements of catechol concentrations were compared between hTyr-injected and control groups using a student's t-test in GraphPad Prism. Similarly, behavioral assessment relied on t-test comparison between groups for latency to feed in the novelty-suppressed feeding task and average percent freezing in the contextual fear assay. Statistical analyses of RNA sequencing data are described above.

Results

Viral infusion of hTyr induces NM-like pigmentation in the LC of mice. To recapitulate NM found endogenously in the human LC, we adapted a viral vector-mediated approach to drive neuronal pigmentation in rodents. TH-Cre mice were stereotaxically infused with AAV5-DIO-hTyr in the LC to drive viral expression of hTyr (**Fig. 1a**), which is known to produce pigment when introduced in rodent SNc DA neurons (Carballo-Carbajal et al., 2019). We found that hTyr expression likewise drove pigmentation of the LC in Cre+ (**Fig. 1b**) but not in Cre- mice (**Fig. 1c,d**) as early as 1 week post-infusion. This pigmentation was visible by gross anatomical inspection (**Fig. 1e**) and brightfield microscopy (**Fig. 1b**). Additionally, we confirmed the presence of melanin in this pigment using Fontana-Masson staining (**Fig. 1f**). We then utilized electron microscopy to compare the pigment granules in our rodent model (**Fig. 1g**) with endogenous NM granules from 16-year-old Rhesus macaque tissue (**Fig. 1h**). Ultrastructural inspection revealed that many of the components known to reside in endogenous NM, including pheomelanin and eumelanin pigments, lipid droplets, and a double membrane, were also present in granules from our rodent model. Together, these results validate the use of hTyr expression to induce NM-like pigmentation in the mouse LC.

NM results in loss of LC fibers but not cell bodies at 1 week. We next sought to determine if rapid accumulation of NM was toxic to LC neurons. To determine whether pigmentation impacted cell body integrity at 1 week post-injection, we performed a count of TH+ and Nissl+ cells in the LC and found no difference between mice that received hTyr or EYFP virus (**Fig. 2a, b**). Given that LC fiber/terminal degeneration precedes cell body loss in AD and PD (Doppler et al., 2021a; Gilvesy et al., 2022), we also assessed NET immunoreactivity, a marker of LC dendrite, axon, and terminal integrity. Consistent with clinical data (Gilvesy et al., 2022) and other rodent models of

LC neurodegeneration (Chalermpalanupap et al., 2018; Butkovich et al., 2020), NET immunoreactivity was visibly reduced in the LC (**Fig. 2c**), as well as in the LC projections to the anterior cingulate cortex (ACC) (**Fig. 2d**) and dentate gyrus (DG) (**Fig. 2e**) of hTyr-injected mice compared to EYFP-injected controls.

NM reduces NE levels throughout the LC network and dysregulates NE turnover in the projection fields at 1 week. Given the loss of LC axons/terminals, we assessed the impact of hTyr-driven pigmentation on tissue levels of catecholamines and their metabolites (**Fig. 3**) to determine if there was a loss of NE tone in target regions. NE was dramatically reduced in the pons, where LC cell bodies reside ($t_{(10)} = 10.14$, $p < 0.0001$), as well as in the prefrontal cortex (PFC; $t_{(10)} = 7.607$, $p < 0.0001$) and hippocampus ($t_{(10)} = 9.735$, $p < 0.0001$), two of the primary projection regions of the LC. Additionally, levels of the primary NE metabolite MHPG were also reduced in the pons ($t_{(10)} = 7.532$, $p < 0.0001$), PFC ($t_{(10)} = 5.152$, $p = 0.0004$) and hippocampus ($t_{(10)} = 3.666$, $p = 0.0043$) (**Fig. 3**). Despite the reduction of total NE and MHPG, the MHPG:NE ratio, which provides an estimate of NE turnover, was significantly increased in the PFC ($t_{(10)} = 2.905$, $p = 0.0157$) and hippocampus ($t_{(10)} = 4.392$, $p = 0.0014$) compared to controls, suggesting adaptations in the LC-NE system (**Fig. 3**). Levels of other amine neuromodulators, including DA, 5-HT, and their respective metabolites, were unchanged with the exception of an increase in DA turnover (metabolite DOPAC:DA) in both the pons ($t_{(10)} = 3.288$, $p = 0.0082$) and PFC ($t_{(10)} = 2.905$, $p = 0.0157$), suggesting that dysfunction resulting from pigmentation of the LC was largely confined to the noradrenergic system at 1 week post-injection (**Table 2**).

NM-positive LC neurons are hyperactive at 1 week. Given the increase in NE turnover, we speculated that at 1 week post-viral infusion, LC neurons burdened with NM were hyperactive. Using *ex vivo* slice electrophysiology, we found that both spontaneous pacemaker (**Fig. 4a**) and current-evoked (**Fig. 4b**) firing were significantly elevated in LC neurons that contained NM from mice that received hTyr virus compared to those from mice that received EYFP virus or other controls (those that received hTyr virus but did not display visible pigment, no virus). For spontaneous firing, one-way ANOVA showed a significant difference between groups ($F_{2,149}$ = 24.02, $p < 0.0001$), and post hoc analysis revealed that the NM-containing LC neurons were hyperactive compared to EYFP controls ($q = 8.81$, $p< 0.0001$) and other controls ($q = 9.26$, $p < 0.0001$). For evoked firing, two-way ANOVA showed a main effect of treatment ($F_{1,99} = 25.35$, $p < 0.0001$), current injection ($F_{14,1386} = 236.20$, $p < 0.0001$), and a treatment x current injection interaction ($F_{14,1386} = 5.49$, $p < 0.0001$). Post hoc analysis revealed that the NM-containing LC neurons were hyperactive compared to EYFP controls at 50 pA ($t = 3.40$, $p < 0.01$), 100 pA ($t = 4.19$, $p < 0.001$), 140 pA ($t = 4.74$, $p < 0.0001$), 180 pA ($t = 5.46$, $p < 0.0001$), 220 pA ($t = 5.27$, $p < 0.0001$), 260 pA ($t = 5.69$, $p < 0.0001$), 300 pA ($t = 4.86$, $p < 0.0001$), 340 pA ($t = 4.59$, $p < 0.0001$), 380 pA ($t = 3.82$, $p < 0.01$), and 500 pA ($t = 2.69$, $p < 0.05$).

The presence of NM in the LC drives novelty-induced anxiety behavior at 1 week. Several prodromal symptoms of PD are regulated by the LC-NE system, and thus are sensitive to the early LC dysfunction which precedes neurodegeneration (Weinshenker, 2018). In particular, we have shown that LC hyperactivity and/or NE signaling is associated with increased anxiety-like behavior in rodent models of AD and PD (Butkovich et al., 2020; Kelberman et al., 2022; Iannitelli et al., 2023b; Kelberman et al., 2023). We assessed the impact of hTyr-induced pigmentation on

LC-associated behaviors, including novelty-induced anxiety, arousal, and cognition, at 1 week post-viral infusion. Consistent with the LC hyperactivity phenotype, we found that hTyr-injected mice were significantly more reactive in the novelty-suppressed feeding task, a novelty-induced stress paradigm commonly used to model anxiety that is sensitive to changes in LC-NE transmission . hTyr-expressing mice took significantly longer than EYFP controls to consume food in the novelty-suppressed feeding task ($t_{(24)} = 2.359$, $p < 0.05$) (**Fig. 5a**). Five hTyr-injected mice (approximately one third) timed out of the task at 15-min, while only one EYFP control mouse timed out of the task, further illustrating an increase in novelty-induced anxiety-like behavior resulting from LC pigmentation. Importantly, hTyr- and EYFP-injected mice displayed no differences in latency to eat in the home cage (data not shown), indicating the experimental group's increased latency to eat during the task resulted from novelty stress behavior rather than changes in satiety state. There were no differences in arousal, as measured by latency to fall asleep following gentle handling (**Fig. 5b**) or associative memory, as measured by freezing in a footshock-associated context (**Fig. 5c**).

NM alters the LC transcriptome at 1 week. To determine how the LC responded to NM accumulation, we assessed the LC-NE mRNA expression using TRAP. Differential expression (DE) analysis was first performed comparing LC (TRAP) and input (whole-tissue) RNA samples for enriched known LC marker genes to verify the method (Mulvey et al., 2018; Iannitelli et al., 2023b). As expected, TRAP fractions were enriched for genes including *Slc6a2*, *Th*, and *Dbh* with log2 fold-change (logFC) values ranging from 2-5. We then sought to examine NM-induced effects on LC-specific and whole hindbrain translatomes by performing DE analyses between genotypes **(Fig. 6a**). The full results of these DE analyses are in **Supplemental Table 1**.

Notably, we observed 10 significant (FDR < 0.05) DE genes (DEGs) between hTyr LC and EYFP LC, but none between input fractions from the two conditions, indicating the specificity of our methods. At nominal significance ($p < 0.05$), we identified 623 genes DE between hTyr input and EYFP input and 813 genes DE between hTyr LC and EYFP LC (**Fig. 6b**); these nominal DEGs were also mostly exclusive to the respective RNA fractions, further supporting LC-specific effects. The top individual genes upregulated in hTyr LC were *Hmox1*, *Sdf2l1*, *Ddit3* (aka GADD34), and *Atf3*; while no genes were significantly downregulated in hTyr LC, those nearest to significance included *Ep400* (FDR=0.144). To understand the functional potential of hTyr-induced gene expression changes in LC, we then utilized GSEA (see *Methods*) with pathways from MsigDB to identify ontologies, cell types, and pathways enriched in genes DE in LC. Top terms enriched in hTyr-LC upregulated genes included pigmentation and multiple facets of ER stress response. (**Fig. 6c** and **Supplemental Table 2**).

To identify transcriptional regulators downstream of hTyr-induced NM aggregation, we also performed GSEA (see *Methods*) on sets of transcription factor (TF) target genes cataloged in several other resources. The top 20 sets were comprised almost exclusively of various annotated target genes of TFs involved in unfolded protein response (UPR), namely *Atf6* and *Xbp1*. Neither of these TFs were differentially expressed between EYFP-LC and hTyr-LC, however. To decipher possible means by which the targets of these TFs could be robustly upregulated without change in TF expression, we identified 61 proteins which have "high confidence" interactions with *Atf6 and/*or *Xbp1* in mouse in StringDB v12.0. Among these interacting proteins, three were significantly DE (all upregulated) in hTyr-LC relative to EYFP-LC: *Ddit3*, *Atf3*, and *Ppp1r15a*. Interestingly, all three of these genes are also implicated in UPR or other forms of endoplasmic

reticulum stress, and two are themselves TFs (Bernstein et al., 2011; Chalour et al., 2018; El Manaa et al., 2021).

Given our findings of UPR in the hTyr LC, along with a substantial body of research implicating this pathway in the detrimental effects of neuropathological aggregates, we next sought to characterize whether AD pathology induced corresponding changes in TF expression in non-NM neurons. Interestingly, the five aforementioned TFs were not DE between bulk RNA from AD and control postmortem brain regions (see *Acknowledgments*), nor were they consistently differentially expressed at the level of cortical cell types identified in a large single-nucleus study of AD (Mathys et al., 2023). To further examine this relationship, we performed the same TF-target GSEA analysis as above, using entorhinal excitatory neuron DE results between early AD pathology/controls and between late/early AD pathology (Mathys et al., 2019). Strikingly, target sets with significant enrichment in early vs. no AD pathology DEGs were negatively enriched (i.e., more highly expressed in controls than early AD), while they were upregulated in late AD relative to early AD (**Supplemental Table 2**). These findings suggest that the UPR pathway induced by NM in the LC is distinct from that induced in neurons more broadly by early pathological aggregates.

Persistent NM accumulation results in neurodegeneration and neuroinflammation in the LC. To assess the consequences of prolonged pigment burden in the LC, we allowed mice to age for several weeks following viral infusion. By 6-10 weeks, we observed a catastrophic loss of LC cell bodies and dendrites, as measured by TH immunoreactivity (**Fig. 7**). The most densely pigmented sub-regions of the LC displayed the most profound cell loss, recapitulating the pattern of neurodegeneration reported in PD (Mann and Yates, 1983b). This neurodegeneration was

accompanied by a profound increase in GFAP immunoreactivity, indicating that astrocytes were reacting to and infiltrating the space vacated by dying NE neurons. Although only a few LC neurons remain at these time points, pigmented granules persisted in the LC region and were also visible beyond its typical confines. Taken together, these data suggest that pigmented granules persist following the death of their host neurons, and in fact may spread to adjacent tissue.

To more fully characterize the ultrastructural composition and distribution of NM in this model over time, we performed electron microscopy on LC tissue. As previously reported for natural human NM, the hTyr-induced NM aggregates were characterized as clusters made up of irregularly shaped granules of various electron density and sizes and lipid droplets. Overall, the clusters of NM were found in neuronal cell bodies (**Fig. 8a,c**), large membrane-delimited neuropil aggregates (**Fig. 8b,d,f**), and glial cells (**Fig. 8e,g**). To determine the phenotype of the neuronal profiles that contained NM, some sections were immunostained for TH to mark LC-NE neurons, while others were labeled for either the astrocytic marker GFAP or the microglia marker IBA-1. As shown in **Fig. 8c**, some TH-positive cell bodies and dendritic profiles were enriched in NM, confirming that NM is found within noradrenergic neurons in the LC.

Regarding glial expression, our observations revealed clear examples of NM aggregates within IBA-1-positive microglia cell bodies (**Fig. 8e,g**), but not in GFAP-positive astrocytes (**Fig. 8f**). However, in some instances, GFAP-positive processes were closely apposed to NM-containing profiles (**Fig. 8f**). We speculated that the persistence of NM in the LC region after many of the NE neurons were lost could be explained by glial engulfment. To test this idea, we counted the total number of neuronal and glial profiles that contained NM in the tissue and calculated the ratio of glia:neuron profile labeling. As shown in **Fig. 8h**, this ratio increased with the length of the post-viral infusion period, from ~5% at 1 week to ~25% at 10 weeks. These data suggest that

NM initially accumulates in LC-NE neurons, but gradually invades the LC neuropil following release upon neuronal death, where it is engulfed by microglia. NM was absent in controls (i.e. mice that received EYFP virus or no virus; **Fig. 8h** and data not shown). With the use of serial EM images (**Figs. 8i-k**, and **Figs. 8m-p**) and the 3D reconstruction approach (**Figs. 8l, q**) we have obtained 3D models of microglia cells (**Fig. 8q**) and their process (**Fig. 8l**) that allowed the spatial visualization of the NM clusters **(Fig. 8l)** and the complete 3D visualization of microglia cells. These 3D images have shown that a large volume of the microglia cytoplasm is occupied by multiple NM clusters and other cytoplasm inclusions of degenerated axonal profiles, and that some processes of iGFAP-positive astrocytes are covering partially the surface the cell (**Figs. 8l, q; Supplemental Video 1**). One limitation of our analysis is that because much of the NM was associated with degenerating neuronal elements (e.g. dendrites) at later time points, it was difficult to discern "intracellular" vs "extracellular" localization with confidence. Given that most of the LC-NE neurons were dead by 6-10 weeks, we assume that much of it was no longer associated with intact cells and was accessible to invading glial at these time points.

Loss of LC neurons depletes NE levels in the brainstem and projection regions and dysregulates NE turnover.

Following pigment-mediated LC degeneration at 6 weeks post-infusion, we re-assessed tissue catecholamine levels. In line with the 1-week data, we found an even greater decrease in NE in the pons ($t_{(9)}$ = 10.23, $p < 0.0001$;), PFC ($t_{(9)}$ = 9.745, $p < 0.0001$), and hippocampus ($t_{(9)}$ = 12.83, < 0.0001) of hTyr-injected mice as compared to EYFP controls (**Fig. 9**). Similarly, we found a decrease in MHPG in the pons ($t_{(9)}$ = 9.489, $p < 0.0001$), PFC ($t_{(9)}$ = 7.659, $p < 0.0001$), and hippocampus ($t_{(9)}$ = 8.207, $p < 0.0001$) (**Fig. 9**). While NE turnover (MHPG:NE) was decreased in

the pons ($t_{(9)}$ = 4.427, p = 0.0017), the increased NE turnover seen in projection regions at 1 week persisted in the PFC ($t_{(9)}$ = 3.11, p = 0.0125) and hippocampus ($t_{(9)}$ = 2.697, p = 0.0245) at 6 weeks (**Fig. 9**). Furthermore, DA turnover was increased in the hippocampus of hTyr-injected animals ($t_{(9)}$ = 2.623, p = 0.0277), likely driven by an increase of the metabolite DOPAC ($t_{(9)}$ = 3.079, p = 0.0132). No changes in 5-HT, metabolite 5-HIAA, or turnover was found in any region at 6 weeks (**Table 2**).

Pigment-mediated neurodegeneration has no behavioral effects at 6-10 weeks. Despite the catastrophic loss of LC neurons and decrease in neurotransmitter levels at 6-10 weeks in mice with NM accumulation, we did not observe any significant differences in behavior compared to mice that received EYFP virus. Notably, novelty-induced anxiety, which was increased in hTyr mice at 1-week, did not differ statistically between groups at 6- or 10-weeks (**Fig. 10a,d**). Pigment-expressing mice also displayed no differences in sleep latency (**Fig. 10b,e**) or contextual fear conditioning (**Fig. 10c,f**).

Discussion

The present study characterized the impact of hTyr-induced NM in the LC of mice, allowing the determination of causal relationships between NM accumulation in noradrenergic neurons, LC-NE integrity and activity, and the development of non-motor symptoms reminiscent of prodromal AD and PD in humans. The expression of NM driven by viral delivery of hTyr is consistent with prior work focused on the SN (Carballo-Carbajal et al., 2019). In our model, neuronal dysfunction was evident as early as 1-week post-infusion. Even at this early time point, we found dramatically decreased NET immunoreactivity in the pons, PFC, and hippocampus of hTyr mice compared to

controls, suggesting loss of fiber/terminal integrity, but no difference in the number of noradrenergic or total LC cell bodies. These findings are consistent with other reports of early LC axon loss in neurodegenerative diseases (Weinshenker, 2018; Doppler et al., 2021b; Gilvesy et al., 2022). Concurrent with fiber loss was depletion of NE and its primary metabolite MHPG in the hippocampus and PFC. We also found elevated MHPG:NE ratio, a measure of NE turnover, in projection regions, suggesting increased release from surviving LC fibers described in rodents (Hallman and Jonsson, 1984; Iannitelli et al., 2022) and humans (Francis et al., 1985; Raskind et al., 1999; Jacobs et al., 2021) with LC neurodegeneration. Using slice electrophysiology, we found that LC-NE neurons containing NM were hyperactive, including increases in both spontaneous and evoked firing. Excessive NE transmission is a common feature of compromised LC neurons, and can occur at the cell body, terminal, and/or postsynaptic receptor level, depending on the nature of the insult (Butkovich et al., 2020; Kelly et al., 2021; Iannitelli et al., 2023b; Kelberman et al., 2023; Wang et al., 2025). We speculate that this hyperactivity is not a direct result of pathology per se, but rather a compensatory response to damage in an effort to maintain normal NE transmission, reminiscent of compensatory LC hyperactivity following chronic inhibition by opioids (Maldonado, 1997; Mazei-Robison and Nestler, 2012).

A NE hyperactivity phenotype is congruent with the LC dysfunction seen in prodromal AD and PD (Weinshenker, 2018). NM-expressing mice displayed elevated novelty-induced anxiety-like behavior at 1 week, indicating that the compensatory LC-NE hyperactivity has behavioral consequences (Lustberg et al., 2020; Kelberman et al., 2022; Iannitelli et al., 2023b). The disappearance of the anxiety phenotype at later time points when the LC was completely degenerated is consistent with this interpretation. It was somewhat surprising that there was no effect on this hyperactivity on sleep latency, as NE transmission promotes arousal (Carter et al.,

2010; Porter-Stransky et al., 2019; Poe et al., 2020). Sleep is a complex process controlled by many brain regions and neurotransmitters, and it is possible that other circuits are compensating in response to the LC hyperactivity in this case.

In the rat hTyr model, NM accumulation induced a general proteostasis failure in SNc neurons, and enhancing proteostasis via overexpression of transcription factor EF (TFEB) attenuated NM-induced degeneration (Carballo-Carbajal et al., 2019). RNA-seq of the hTyr-expressing LC revealed large impacts of induced NM production on the transcriptome of LC neurons, markedly converging on UPR pathways. Notably, target genes of UPR TFs *Atf6* and *Xbp1* are the most robustly upregulated in hTyr-LC, though these two TFs themselves do not show a change in expression compared to EYFP-LC. Rather, several TFs which interact with *Atf6* and/or *Xbp1* and which are also members of the UPR pathway are upregulated, suggesting that NM induces *Atf6*- and *Xbp1*-associated genes through activity of interacting TFs (*Ddit3*, *Atf3*). Moreover, we find that the targets of these same TFs are *downregulated* in excitatory neurons of the entorhinal cortex in early AD (Mathys et al., 2019), suggesting the UPR pathway induced by NM may counter neuronal UPR pathway effects of early proteinopathy. Notably, *XBP1* overexpression enables human neuron survival in the presence of ordinarily cell-fatal amounts of Aβ (Duran-Aniotz et al., 2023), suggesting that induction of these TFs in LC in our model represents an adaptive neuronal response to the presence of NM. *Atf6* and *Xbp1*, whose targets appear to be upregulated by NM, are attributed to the “adaptive”, rather than pro-apoptotic, arm of the UPR (Hetz et al., 2020). Consistent with the observation that LC cell bodies can persist for years with high tau burden (Braak et al., 2011), our findings suggest a potential mechanism by which NM acts as *both* a cellular insult *and* a neuroprotectant. For example, in responding to accumulating NM, the LC upregulates *Atf3/Atf6/Xbp1/Ddit3* or their targets,

allowing the cell to tolerate the effects of NM (to a limited extent) while simultaneously inducing a molecular state that is protective against the toxic effects of protein aggregates found in neurodegenerative diseases.

Substantial cell death and neuroinflammation in the LC were evident by 6-10 weeks post-viral infusion. Transgenic expression of hTyr driven by the TH promoter similarly provokes LC cell death in mice, albeit on a slower time scale (Laguna et al., 2024). The rapid NM accumulation and toxicity in our model likely reflects the higher expression from a virus compared to the transgene. Dense NM persisted in the region even when the LC was almost completely degenerated, suggesting that it had been released by dying neurons and was either extracellular or had been taken up by other cells. At the gross immunofluorescent level, the astrocyte response was dominant, but while electron microscopic analysis showed many astrocyte processes closely apposed to NM granules, only microglia appeared competent to engulf the NM. Extracellular NM-induced activation of microglia has been reported in human postmortem tissue, animal models, and cell culture (Zecca et al., 2003; Zecca et al., 2008a; Zhang et al., 2011). Neuroinflammation is a well-appreciated aspect of AD and PD that is influenced by the LC-NE system (Chalermpalanupap et al., 2013; Feinstein et al., 2016; Giorgi et al., 2020; Mercan and Heneka, 2022; Tansey et al., 2022). Our data suggest that the release of pigmentation from degenerating LC neurons contributes to the neuroimmune response.

Due to the catastrophic loss of NE cell bodies and deteriorating state of the ones that persisted, we were unable to directly assess LC activity at the 6-10 week time points. Using HPLC as a proxy, we found increased NE turnover in LC terminal regions at 6 weeks suggestive of compensatory NE release from surviving terminals, similar to the 1 week data. However, this did not correspond with increases in anxiety-like behavior, presumably because NE, which is required

for novelty-suppressed feeding (Lustberg et al., 2020), was barely above the limit of detection. There were no differences between groups in sleep latency, novelty-induced anxiety, or contextual fear memory. The loss of an anxiety-like phenotype at 6-weeks may be explained by a near-total loss of LC-NE, which is required for this behavior (Lustberg et al., 2020). While contextual fear memory should also require LC innervation of the hippocampus (McGaugh, 2013), recent studies have also implicated DA in hippocampal function and fear memory (Likhtik and Johansen, 2019; Stubbendorff and Stevenson, 2021). Thus, the increase in DA turnover in the hippocampus at 6-weeks may account for the lack of behavioral differences observed in the contextual fear task.

The present study provides novel insights into the consequences of NM accumulation in rodent LC-NE neurons. We found that pigment expression dysregulates LC neurons on a cellular and molecular level at 1 week, triggering an anxiety-like phenotype reminiscent of prodromal AD and PD. As the pigment accumulates, immune response and neurodegeneration ensue. By 6-10 weeks post-infusion, the LC has nearly entirely degenerated and most of the NM is contained in deteriorating neuronal elements, the extracellular neuropil, and microglia. An important aspect of our study is that hTyr overexpression drives extremely rapid NM accumulation (weeks) compared to natural NM accumulation in humans (decades), which likely dramatically accelerates its ability to overwhelm cellular machinery and lead to cell death. In this respect, our approach shares the same limitation as all rodent models of neurodegenerative disease. Nevertheless, there is ample evidence that the same processes contribute to LC neuron dysregulation and demise in AD and PD. For example, LC neurons with the highest NM content are disproportionally lost in PD (Mann and Yates, 1983b). It was previously reported that hTyr-expressing SN-DA neurons took many months to degenerate (Carballo-Carbajal et al., 2019). It is not clear whether this reflects differences with our model in the virus itself (AAV2 vs Cre-dependent AAV5), species (rat vs

mouse), or a true greater vulnerability of LC neurons. Thus, direct comparisons will be needed to answer this question. Ultimately, this model of pigment induction in rodent catecholamine neurons may be critical for uncovering the role NM plays in the early vulnerability of LC neurons in AD and PD.

Author Contributions

A.F.I. designed and performed research, analyzed data, and wrote the manuscript. L.H. designed and performed researched, analyzed data, and edited the manuscript. M.M.T. designed and performed researched. B.M. assisted with research design and data analysis. H.E.B. performed research and analyzed data. M.T. designed and performed research, A.K. designed and performed research, L.C.L. assisted with research design and analysis. A.L.S. performed research and analyzed data. J-F.P. performed research and analyzed data. R.V. performed research and edited the manuscript. A.S. performed research and analyzed data. S.A.S. assisted with research design and data analysis. K.M. assisted with data analysis. K.E.M. performed research and analyzed data. J.D.D. assisted with research design and contributed analytic tools. Y.S. assisted with research design and data analysis. M.J.B. designed and performed research, analyzed data, and wrote the manuscript. D.W. designed research, analyzed data, and wrote the manuscript.

Acknowledgements

This work was supported by a National Institutes of Health (NIH) National Institute of Environmental Health Sciences Training Grant (ES12870) and a NIH D-SPAN F99/K00 Award from the National Institute of Neurological Disorders and Stroke (NS129168) to A.F.I, as well as RF1 awards from the National Institute on Aging (AG079199 to D.W. and AG061175 to D.W.

and M.J.B.). This study was supported in part by the Emory HPLC Bioanalytical Core (EHBC), which is subsidized by the Emory University School of Medicine and is one of the Emory Integrated Core Facilities. Additional support was provided by the Georgia Clinical & Translational Science Alliance of the National Institutes of Health under Award Number UL1TR002378. The results published here are in whole or in part based on data obtained from Agora, a platform initially developed by the NIA-funded AMP-AD consortium that shares evidence in support of AD target discovery. Agora is available at: doi:10.57718/agora.adknowledgeportal.

References

Barden H, Levine S (1983) Histochemical observations on rodent brain melanin. Brain Res Bull 10:847-851.

Bernstein AI, Garrison SP, Zambetti GP, O'Malley KL (2011) 6-OHDA generated ROS induces DNA damage and p53- and PUMA-dependent cell death. Mol Neurodegener 6:2.

Bondareff W, Mountjoy CQ, Roth M (1982) Loss of neurons of origin of the adrenergic projection to cerebral cortex (nucleus locus ceruleus) in senile dementia. Neurology 32:164-168.

Braak E, Sandmann-Keil D, Rub U, Gai WP, de Vos RA, Steur EN, Arai K, Braak H (2001) alpha-synuclein immunopositive Parkinson's disease-related inclusion bodies in lower brain stem nuclei. Acta Neuropathol 101:195-201.

Braak H, Del Tredici K (2011a) Alzheimer's pathogenesis: is there neuron-to-neuron propagation? Acta Neuropathol 121:589-595.

Braak H, Del Tredici K (2011b) The pathological process underlying Alzheimer's disease in individuals under thirty. Acta Neuropathol 121:171-181.

Braak H, Thal DR, Ghebremedhin E, Del Tredici K (2011) Stages of the pathologic process in Alzheimer disease: age categories from 1 to 100 years. J Neuropathol Exp Neurol 70:960-969.

Branch SY, Beckstead MJ (2012) Methamphetamine produces bidirectional, concentration-dependent effects on dopamine neuron excitability and dopamine-mediated synaptic currents. J Neurophysiol 108:802-809.

Bueicheku E, Diez I, Kim CM, Becker JA, Koops EA, Kwong K, Papp KV, Salat DH, Bennett DA, Rentz DM, Sperling RA, Johnson KA, Sepulcre J, Jacobs HIL (2024)

Spatiotemporal patterns of locus coeruleus integrity predict cortical tau and cognition. Nat Aging 4:625-637.

Bush WD, Garguilo J, Zucca FA, Albertini A, Zecca L, Edwards GS, Nemanich RJ, Simon JD (2006) The surface oxidation potential of human neuromelanin reveals a spherical architecture with a pheomelanin core and a eumelanin surface. Proc Natl Acad Sci U S A 103:14785-14789.

Butkovich LM, Houser MC, Chalermpalanupap T, Porter-Stransky KA, Iannitelli AF, Boles JS, Lloyd GM, Coomes AS, Eidson LN, De Sousa Rodrigues ME, Oliver DL, Kelly SD, Chang J, Bengoa-Vergniory N, Wade-Martins R, Giasson BI, Joers V, Weinshenker D, Tansey MG (2020) Transgenic Mice Expressing Human alpha-Synuclein in Noradrenergic Neurons Develop Locus Ceruleus Pathology and Nonmotor Features of Parkinson's Disease. J Neurosci 40:7559-7576.

Carballo-Carbajal I, Laguna A, Romero-Gimenez J, Cuadros T, Bove J, Martinez-Vicente M, Parent A, Gonzalez-Sepulveda M, Penuelas N, Torra A, Rodriguez-Galvan B, Ballabio A, Hasegawa T, Bortolozzi A, Gelpi E, Vila M (2019) Brain tyrosinase overexpression implicates age-dependent neuromelanin production in Parkinson's disease pathogenesis. Nat Commun 10:973.

Carter ME, Yizhar O, Chikahisa S, Nguyen H, Adamantidis A, Nishino S, Deisseroth K, de Lecea L (2010) Tuning arousal with optogenetic modulation of locus coeruleus neurons. Nat Neurosci 13:1526-1533.

Chalermpalanupap T, Schroeder JP, Rorabaugh JM, Liles LC, Lah JJ, Levey AI, Weinshenker D (2018) Locus Coeruleus Ablation Exacerbates Cognitive Deficits, Neuropathology, and Lethality in P301S Tau Transgenic Mice. J Neurosci 38:74-92.

Chalermpalanupap T, Kinkead B, Hu WT, Kummer MP, Hammerschmidt T, Heneka MT, Weinshenker D, Levey AI (2013) Targeting norepinephrine in mild cognitive impairment and Alzheimer's disease. Alzheimers Res Ther 5:21.

Chalour N, Maoui A, Rat P, Massicot F, Dutot M, Faussat AM, Devevre E, Limb A, Warnet JM, Treton J, Dinet V, Mascarelli F (2018) AbetaPP-induced UPR Transcriptomic Signature of Glial Cells to Oxidative Stress as an Adaptive Mechanism to Preserve Cell Function and Survival. Curr Alzheimer Res 15:643-654.

Clarke DJB, Marino GB, Deng EZ, Xie Z, Evangelista JE, Ma'ayan A (2024) Rummagene: massive mining of gene sets from supporting materials of biomedical research publications. Commun Biol 7:482.

Del Tredici K, Rub U, De Vos RA, Bohl JR, Braak H (2002) Where does parkinson disease pathology begin in the brain? J Neuropathol Exp Neurol 61:413-426.

Doppler CEJ, Kinnerup MB, Brune C, Farrher E, Betts M, Fedorova TD, Schaldemose JL, Knudsen K, Ismail R, Seger AD, Hansen AK, Staer K, Fink GR, Brooks DJ, Nahimi A, Borghammer P, Sommerauer M (2021a) Regional locus coeruleus degeneration is uncoupled from noradrenergic terminal loss in Parkinson's disease. Brain 144:2732-2744.

Doppler CEJ, Kinnerup MB, Brune C, Farrher E, Betts M, Fedorova TD, Schaldemose JL, Knudsen K, Ismail R, Seger AD, Hansen AK, Staer K, Fink GR, Brooks DJ, Nahimi A, Borghammer P, Sommerauer M (2021b) Regional locus coeruleus degeneration is uncoupled from noradrenergic terminal loss in Parkinson's disease. Brain.

Duran-Aniotz C et al. (2023) The unfolded protein response transcription factor XBP1s ameliorates Alzheimer's disease by improving synaptic function and proteostasis. Mol Ther 31:2240-2256.

Ehrenberg AJ, Suemoto CK, Franca Resende EP, Petersen C, Leite REP, Rodriguez RD, Ferretti-Rebustini REL, You M, Oh J, Nitrini R, Pasqualucci CA, Jacob-Filho W, Kramer JH, Gatchel JR, Grinberg LT (2018) Neuropathologic Correlates of Psychiatric Symptoms in Alzheimer's Disease. J Alzheimers Dis 66:115-126.

Ehrenberg AJ, Nguy AK, Theofilas P, Dunlop S, Suemoto CK, Di Lorenzo Alho AT, Leite RP, Diehl Rodriguez R, Mejia MB, Rub U, Farfel JM, de Lucena Ferretti-Rebustini RE, Nascimento CF, Nitrini R, Pasquallucci CA, Jacob-Filho W, Miller B, Seeley WW, Heinsen H, Grinberg LT (2017) Quantifying the accretion of hyperphosphorylated tau in the locus coeruleus and dorsal raphe nucleus: the pathological building blocks of early Alzheimer's disease. Neuropathol Appl Neurobiol 43:393-408.

El Manaa W, Duplan E, Goiran T, Lauritzen I, Vaillant Beuchot L, Lacas-Gervais S, Morais VA, You H, Qi L, Salazar M, Ozcan U, Chami M, Checler F, Alves da Costa C (2021) Transcription- and phosphorylation-dependent control of a functional interplay between XBP1s and PINK1 governs mitophagy and potentially impacts Parkinson disease pathophysiology. Autophagy 17:4363-4385.

Falgas N, Pena-Gonzalez M, Val-Guardiola A, Perez-Millan A, Guillen N, Sarto J, Esteller D, Bosch B, Fernandez-Villullas G, Tort-Merino A, Maya G, Auge JM, Iranzo A, Balasa M, Llado A, Morales-Ruiz M, Bargallo N, Munoz-Moreno E, Grinberg LT, Sanchez-Valle R (2024) Locus coeruleus integrity and neuropsychiatric symptoms in a cohort of early- and late-onset Alzheimer's disease. Alzheimers Dement.

Feinstein DL, Kalinin S, Braun D (2016) Causes, consequences, and cures for neuroinflammation mediated via the locus coeruleus: noradrenergic signaling system. J Neurochem 139 Suppl 2:154-178.

Francis PT, Palmer AM, Sims NR, Bowen DM, Davison AN, Esiri MM, Neary D, Snowden JS, Wilcock GK (1985) Neurochemical studies of early-onset Alzheimer's disease. Possible influence on treatment. N Engl J Med 313:7-11.

German DC, Manaye KF, White CL, 3rd, Woodward DJ, McIntire DD, Smith WK, Kalaria RN, Mann DM (1992) Disease-specific patterns of locus coeruleus cell loss. Ann Neurol 32:667-676.

Ghosh A, Torraville SE, Mukherjee B, Walling SG, Martin GM, Harley CW, Yuan Q (2019) An experimental model of Braak's pretangle proposal for the origin of Alzheimer's disease: the role of locus coeruleus in early symptom development. Alzheimers Res Ther 11:59.

Gilvesy A, Husen E, Magloczky Z, Mihaly O, Hortobagyi T, Kanatani S, Heinsen H, Renier N, Hokfelt T, Mulder J, Uhlen M, Kovacs GG, Adori C (2022) Spatiotemporal characterization of cellular tau pathology in the human locus coeruleus-pericoerulear complex by three-dimensional imaging. Acta Neuropathol 144:651-676.

Giorgi FS, Biagioni F, Galgani A, Pavese N, Lazzeri G, Fornai F (2020) Locus Coeruleus Modulates Neuroinflammation in Parkinsonism and Dementia. Int J Mol Sci 21.

Hallman H, Jonsson G (1984) Monoamine neurotransmitter metabolism in microencephalic rat brain after prenatal methylazoxymethanol treatment. Brain Res Bull 13:383-389.

Han H, Cho JW, Lee S, Yun A, Kim H, Bae D, Yang S, Kim CY, Lee M, Kim E, Lee S, Kang B, Jeong D, Kim Y, Jeon HN, Jung H, Nam S, Chung M, Kim JH, Lee I (2018) TRRUST v2: an expanded reference database of human and mouse transcriptional regulatory interactions. Nucleic Acids Res 46:D380-D386.

Heneka MT, Ramanathan M, Jacobs AH, Dumitrescu-Ozimek L, Bilkei-Gorzo A, Debeir T, Sastre M, Galldiks N, Zimmer A, Hoehn M, Heiss WD, Klockgether T, Staufenbiel M

(2006) Locus ceruleus degeneration promotes Alzheimer pathogenesis in amyloid precursor protein 23 transgenic mice. J Neurosci 26:1343-1354.

Hetz C, Zhang K, Kaufman RJ (2020) Mechanisms, regulation and functions of the unfolded protein response. Nat Rev Mol Cell Biol 21:421-438.

Hunsley MS, Palmiter RD (2004) Altered sleep latency and arousal regulation in mice lacking norepinephrine. Pharmacol Biochem Behav 78:765-773.

Iannitelli AF, Weinshenker D (2023) Riddles in the dark: Decoding the relationship between neuromelanin and neurodegeneration in locus coeruleus neurons. Neurosci Biobehav Rev 152:105287.

Iannitelli AF, Segal A, Pare JF, Mulvey B, Liles LC, Sloan SA, McCann KE, Dougherty JD, Smith Y, Weinshenker D (2023a) Tyrosinase-induced neuromelanin accumulation triggers rapid dysregulation and degeneration of the mouse locus coeruleus. bioRxiv.

Iannitelli AF, Kelberman MA, Lustberg DJ, Korukonda A, McCann KE, Mulvey B, Segal A, Liles LC, Sloan SA, Dougherty JD, Weinshenker D (2022) The Neurotoxin DSP-4 Dysregulates the Locus Coeruleus-Norepinephrine System and Recapitulates Molecular and Behavioral Aspects of Prodromal Neurodegenerative Disease. bioRxiv:2022.2009.2027.509797.

Iannitelli AF, Kelberman MA, Lustberg DJ, Korukonda A, McCann KE, Mulvey B, Segal A, Liles LC, Sloan SA, Dougherty JD, Weinshenker D (2023b) The Neurotoxin DSP-4 Dysregulates the Locus Coeruleus-Norepinephrine System and Recapitulates Molecular and Behavioral Aspects of Prodromal Neurodegenerative Disease. eNeuro 10.

Iversen LL, Rossor MN, Reynolds GP, Hills R, Roth M, Mountjoy CQ, Foote SL, Morrison JH, Bloom FE (1983) Loss of pigmented dopamine-beta-hydroxylase positive cells from locus coeruleus in senile dementia of Alzheimer's type. Neurosci Lett 39:95-100.

Jacobs HIL, Becker JA, Kwong K, Engels-Dominguez N, Prokopiou PC, Papp KV, Properzi M, Hampton OL, d'Oleire Uquillas F, Sanchez JS, Rentz DM, El Fakhri G, Normandin MD, Price JC, Bennett DA, Sperling RA, Johnson KA (2021) In vivo and neuropathology data support locus coeruleus integrity as indicator of Alzheimer's disease pathology and cognitive decline. Sci Transl Med 13:eabj2511.

Kang SS, Liu X, Ahn EH, Xiang J, Manfredsson FP, Yang X, Luo HR, Liles LC, Weinshenker D, Ye K (2020) Norepinephrine metabolite DOPEGAL activates AEP and pathological Tau aggregation in locus coeruleus. J Clin Invest 130:422-437.

Kang SS, Meng L, Zhang X, Wu Z, Mancieri A, Xie B, Liu X, Weinshenker D, Peng J, Zhang Z, Ye K (2022) Tau modification by the norepinephrine metabolite DOPEGAL stimulates its pathology and propagation. Nat Struct Mol Biol 29:292-305.

Keenan AB, Torre D, Lachmann A, Leong AK, Wojciechowicz ML, Utti V, Jagodnik KM, Kropiwnicki E, Wang Z, Ma'ayan A (2019) ChEA3: transcription factor enrichment analysis by orthogonal omics integration. Nucleic Acids Res 47:W212-W224.

Kelberman MA, Anderson CR, Chlan E, Rorabaugh JM, McCann KE, Weinshenker D (2022) Consequences of Hyperphosphorylated Tau in the Locus Coeruleus on Behavior and Cognition in a Rat Model of Alzheimer's Disease. J Alzheimers Dis 86:1037-1059.

Kelberman MA, Rorabaugh JM, Anderson CR, Marriott A, DePuy SD, Rasmussen K, McCann KE, Weiss JM, Weinshenker D (2023) Age-dependent dysregulation of locus coeruleus firing in a transgenic rat model of Alzheimer's disease. Neurobiol Aging 125:98-108.

Kelly L, Seifi M, Ma R, Mitchell SJ, Rudolph U, Viola KL, Klein WL, Lambert JJ, Swinny JD (2021) Identification of intraneuronal amyloid beta oligomers in locus coeruleus neurons of Alzheimer's patients and their potential impact on inhibitory neurotransmitter receptors and neuronal excitability. Neuropathol Appl Neurobiol 47:488-505.

Korotkevich G, Sukhov V, Budin N, Shpak B, Artyomov MN, Sergushichev A (2021) Fast gene set enrichment analysis. bioRxiv.

Laguna A, Penuelas N, Gonzalez-Sepulveda M, Nicolau A, Arthaud S, Guillard-Sirieix C, Lorente-Picon M, Compte J, Miquel-Rio L, Xicoy H, Liu J, Parent A, Cuadros T, Romero-Gimenez J, Pujol G, Gimenez-Llort L, Fort P, Bortolozzi A, Carballo-Carbajal I, Vila M (2024) Modelling human neuronal catecholaminergic pigmentation in rodents recapitulates age-related neurodegenerative deficits. Nat Commun 15:8819.

Li Y, Wang C, Wang J, Zhou Y, Ye F, Zhang Y, Cheng X, Huang Z, Liu K, Fei G, Zhong C, Zeng M, Jin L (2019) Mild cognitive impairment in de novo Parkinson's disease: A neuromelanin MRI study in locus coeruleus. Mov Disord 34:884-892.

Likhtik E, Johansen JP (2019) Neuromodulation in circuits of aversive emotional learning. Nat Neurosci 22:1586-1597.

Lustberg D, Tillage RP, Bai Y, Pruitt M, Liles LC, Weinshenker D (2020) Noradrenergic circuits in the forebrain control affective responses to novelty. Psychopharmacology (Berl) 237:3337-3355.

Lustberg DJ, Liu JQ, Iannitelli AF, Vanderhoof SO, Liles LC, McCann KE, Weinshenker D (2022) Norepinephrine and dopamine contribute to distinct repetitive behaviors induced by novel odorant stress in male and female mice. Horm Behav 144:105205.

Maldonado R (1997) Participation of noradrenergic pathways in the expression of opiate withdrawal: biochemical and pharmacological evidence. Neurosci Biobehav Rev 21:91-104.

Mann DM, Yates PO (1983a) Pathological basis for neurotransmitter changes in Parkinson's disease. Neuropathol Appl Neurobiol 9:3-19.

Mann DM, Yates PO (1983b) Possible role of neuromelanin in the pathogenesis of Parkinson's disease. Mech Ageing Dev 21:193-203.

Mann DM, Lincoln J, Yates PO, Stamp JE, Toper S (1980) Changes in the monoamine containing neurones of the human CNS in senile dementia. Br J Psychiatry 136:533-541.

Matchett BJ, Grinberg LT, Theofilas P, Murray ME (2021) The mechanistic link between selective vulnerability of the locus coeruleus and neurodegeneration in Alzheimer's disease. Acta Neuropathol 141:631-650.

Mathys H, Davila-Velderrain J, Peng Z, Gao F, Mohammadi S, Young JZ, Menon M, He L, Abdurrob F, Jiang X, Martorell AJ, Ransohoff RM, Hafler BP, Bennett DA, Kellis M, Tsai LH (2019) Single-cell transcriptomic analysis of Alzheimer's disease. Nature 570:332-337.

Mathys H et al. (2023) Single-cell atlas reveals correlates of high cognitive function, dementia, and resilience to Alzheimer's disease pathology. Cell 186:4365-4385 e4327.

Mazei-Robison MS, Nestler EJ (2012) Opiate-induced molecular and cellular plasticity of ventral tegmental area and locus coeruleus catecholamine neurons. Cold Spring Harb Perspect Med 2:a012070.

McGaugh JL (2013) Making lasting memories: remembering the significant. Proc Natl Acad Sci U S A 110 Suppl 2:10402-10407.

Mercan D, Heneka MT (2022) The Contribution of the Locus Coeruleus-Noradrenaline System Degeneration during the Progression of Alzheimer's Disease. Biology (Basel) 11.

Mulvey B, Frye HE, Lintz T, Fass S, Tycksen E, Nelson EC, Moron JA, Dougherty JD (2023) Cnih3 Deletion Dysregulates Dorsal Hippocampal Transcription across the Estrous Cycle. eNeuro 10.

Mulvey B, Bhatti DL, Gyawali S, Lake AM, Kriaucionis S, Ford CP, Bruchas MR, Heintz N, Dougherty JD (2018) Molecular and Functional Sex Differences of Noradrenergic Neurons in the Mouse Locus Coeruleus. Cell Rep 23:2225-2235.

Murchison CF, Zhang XY, Zhang WP, Ouyang M, Lee A, Thomas SA (2004) A distinct role for norepinephrine in memory retrieval. Cell 117:131-143.

Pletnikova O, Kageyama Y, Rudow G, LaClair KD, Albert M, Crain BJ, Tian J, Fowler D, Troncoso JC (2018) The spectrum of preclinical Alzheimer's disease pathology and its modulation by ApoE genotype. Neurobiol Aging 71:72-80.

Poe GR, Foote S, Eschenko O, Johansen JP, Bouret S, Aston-Jones G, Harley CW, Manahan-Vaughan D, Weinshenker D, Valentino R, Berridge C, Chandler DJ, Waterhouse B, Sara SJ (2020) Locus coeruleus: a new look at the blue spot. Nat Rev Neurosci 21:644-659.

Porter-Stransky KA, Centanni SW, Karne SL, Odil LM, Fekir S, Wong JC, Jerome C, Mitchell HA, Escayg A, Pedersen NP, Winder DG, Mitrano DA, Weinshenker D (2019) Noradrenergic Transmission at Alpha1-Adrenergic Receptors in the Ventral Periaqueductal Gray Modulates Arousal. Biol Psychiatry 85:237-247.

Prediger RD, Matheus FC, Schwarzbold ML, Lima MM, Vital MA (2012) Anxiety in Parkinson's disease: a critical review of experimental and clinical studies. Neuropharmacology 62:115-124.

Prokopiou PC, Engels-Dominguez N, Papp KV, Scott MR, Schultz AP, Schneider C, Farrell ME, Buckley RF, Quiroz YT, El Fakhri G, Rentz DM, Sperling RA, Johnson KA, Jacobs HIL (2022) Lower novelty-related locus coeruleus function is associated with Abeta-related cognitive decline in clinically healthy individuals. Nat Commun 13:1571.

Raskind MA, Peskind ER, Holmes C, Goldstein DS (1999) Patterns of cerebrospinal fluid catechols support increased central noradrenergic responsiveness in aging and Alzheimer's disease. Biol Psychiatry 46:756-765.

Remy P, Doder M, Lees A, Turjanski N, Brooks D (2005) Depression in Parkinson's disease: loss of dopamine and noradrenaline innervation in the limbic system. Brain 128:1314-1322.

Rorabaugh JM, Chalermpalanupap T, Botz-Zapp CA, Fu VM, Lembeck NA, Cohen RM, Weinshenker D (2017) Chemogenetic locus coeruleus activation restores reversal learning in a rat model of Alzheimer's disease. Brain 140:3023-3038.

Smyth GK, Michaud J, Scott HS (2005) Use of within-array replicate spots for assessing differential expression in microarray experiments. Bioinformatics 21:2067-2075.

Sommerauer M, Fedorova TD, Hansen AK, Knudsen K, Otto M, Jeppesen J, Frederiksen Y, Blicher JU, Geday J, Nahimi A, Damholdt MF, Brooks DJ, Borghammer P (2018) Evaluation of the noradrenergic system in Parkinson's disease: an 11C-MeNER PET and neuromelanin MRI study. Brain 141:496-504.

Stubbendorff C, Stevenson CW (2021) Dopamine regulation of contextual fear and associated neural circuit function. Eur J Neurosci 54:6933-6947.

Subramanian A, Tamayo P, Mootha VK, Mukherjee S, Ebert BL, Gillette MA, Paulovich A, Pomeroy SL, Golub TR, Lander ES, Mesirov JP (2005) Gene set enrichment analysis: a

knowledge-based approach for interpreting genome-wide expression profiles. Proc Natl Acad Sci U S A 102:15545-15550.

Sulzer D, Mosharov E, Talloczy Z, Zucca FA, Simon JD, Zecca L (2008) Neuronal pigmented autophagic vacuoles: lipofuscin, neuromelanin, and ceroid as macroautophagic responses during aging and disease. J Neurochem 106:24-36.

Sulzer D, Bogulavsky J, Larsen KE, Behr G, Karatekin E, Kleinman MH, Turro N, Krantz D, Edwards RH, Greene LA, Zecca L (2000) Neuromelanin biosynthesis is driven by excess cytosolic catecholamines not accumulated by synaptic vesicles. Proc Natl Acad Sci U S A 97:11869-11874.

Tansey MG, Wallings RL, Houser MC, Herrick MK, Keating CE, Joers V (2022) Inflammation and immune dysfunction in Parkinson disease. Nat Rev Immunol 22:657-673.

Theofilas P, Ehrenberg AJ, Dunlop S, Di Lorenzo Alho AT, Nguy A, Leite REP, Rodriguez RD, Mejia MB, Suemoto CK, Ferretti-Rebustini REL, Polichiso L, Nascimento CF, Seeley WW, Nitrini R, Pasqualucci CA, Jacob Filho W, Rueb U, Neuhaus J, Heinsen H, Grinberg LT (2017) Locus coeruleus volume and cell population changes during Alzheimer's disease progression: A stereological study in human postmortem brains with potential implication for early-stage biomarker discovery. Alzheimers Dement 13:236-246.

Tillage RP, Wilson GE, Liles LC, Holmes PV, Weinshenker D (2020a) Chronic Environmental or Genetic Elevation of Galanin in Noradrenergic Neurons Confers Stress Resilience in Mice. J Neurosci 40:7464-7474.

Tillage RP, Sciolino NR, Plummer NW, Lustberg D, Liles LC, Hsiang M, Powell JM, Smith KG, Jensen P, Weinshenker D (2020b) Elimination of galanin synthesis in noradrenergic

neurons reduces galanin in select brain areas and promotes active coping behaviors. Brain Struct Funct 225:785-803.

Vazey EM, Aston-Jones G (2012) The emerging role of norepinephrine in cognitive dysfunctions of Parkinson's disease. Front Behav Neurosci 6:48.

Wang ZM, Grinevich V, Meeker WR, Zhang J, Messi ML, Budygin E, Delbono O (2025) Early signs of neuron autonomous and non-autonomous hyperexcitability in locus coeruleus noradrenergic neurons of a mouse model of tauopathy and Alzheimer's disease. Acta Physiol (Oxf) 241:e70022.

Weinshenker D (2018) Long Road to Ruin: Noradrenergic Dysfunction in Neurodegenerative Disease. Trends Neurosci 41:211-223.

Williams JT, North RA, Shefner SA, Nishi S, Egan TM (1984) Membrane properties of rat locus coeruleus neurones. Neuroscience 13:137-156.

Xie Z, Bailey A, Kuleshov MV, Clarke DJB, Evangelista JE, Jenkins SL, Lachmann A, Wojciechowicz ML, Kropiwnicki E, Jagodnik KM, Jeon M, Ma'ayan A (2021) Gene Set Knowledge Discovery with Enrichr. Curr Protoc 1:e90.

Ye R, O'Callaghan C, Rua C, Hezemans FH, Holland N, Malpetti M, Jones PS, Barker RA, Williams-Gray CH, Robbins TW, Passamonti L, Rowe J (2022) Locus Coeruleus Integrity from 7 T MRI Relates to Apathy and Cognition in Parkinsonian Disorders. Mov Disord 37:1663-1672.

Zarow C, Lyness SA, Mortimer JA, Chui HC (2003) Neuronal loss is greater in the locus coeruleus than nucleus basalis and substantia nigra in Alzheimer and Parkinson diseases. Arch Neurol 60:337-341.

Zecca L, Zucca FA, Wilms H, Sulzer D (2003) Neuromelanin of the substantia nigra: a neuronal black hole with protective and toxic characteristics. Trends Neurosci 26:578-580.

Zecca L, Wilms H, Geick S, Claasen JH, Brandenburg LO, Holzknecht C, Panizza ML, Zucca FA, Deuschl G, Sievers J, Lucius R (2008a) Human neuromelanin induces neuroinflammation and neurodegeneration in the rat substantia nigra: implications for Parkinson's disease. Acta Neuropathol 116:47-55.

Zecca L, Stroppolo A, Gatti A, Tampellini D, Toscani M, Gallorini M, Giaveri G, Arosio P, Santambrogio P, Fariello RG, Karatekin E, Kleinman MH, Turro N, Hornykiewicz O, Zucca FA (2004) The role of iron and copper molecules in the neuronal vulnerability of locus coeruleus and substantia nigra during aging. Proc Natl Acad Sci U S A 101:9843-9848.

Zecca L, Bellei C, Costi P, Albertini A, Monzani E, Casella L, Gallorini M, Bergamaschi L, Moscatelli A, Turro NJ, Eisner M, Crippa PR, Ito S, Wakamatsu K, Bush WD, Ward WC, Simon JD, Zucca FA (2008b) New melanic pigments in the human brain that accumulate in aging and block environmental toxic metals. Proc Natl Acad Sci U S A 105:17567-17572.

Zhang W, Phillips K, Wielgus AR, Liu J, Albertini A, Zucca FA, Faust R, Qian SY, Miller DS, Chignell CF, Wilson B, Jackson-Lewis V, Przedborski S, Joset D, Loike J, Hong JS, Sulzer D, Zecca L (2011) Neuromelanin activates microglia and induces degeneration of dopaminergic neurons: implications for progression of Parkinson's disease. Neurotox Res 19:63-72.

Zweig RM, Cardillo JE, Cohen M, Giere S, Hedreen JC (1993) The locus ceruleus and dementia in Parkinson's disease. Neurology 43:986-991.

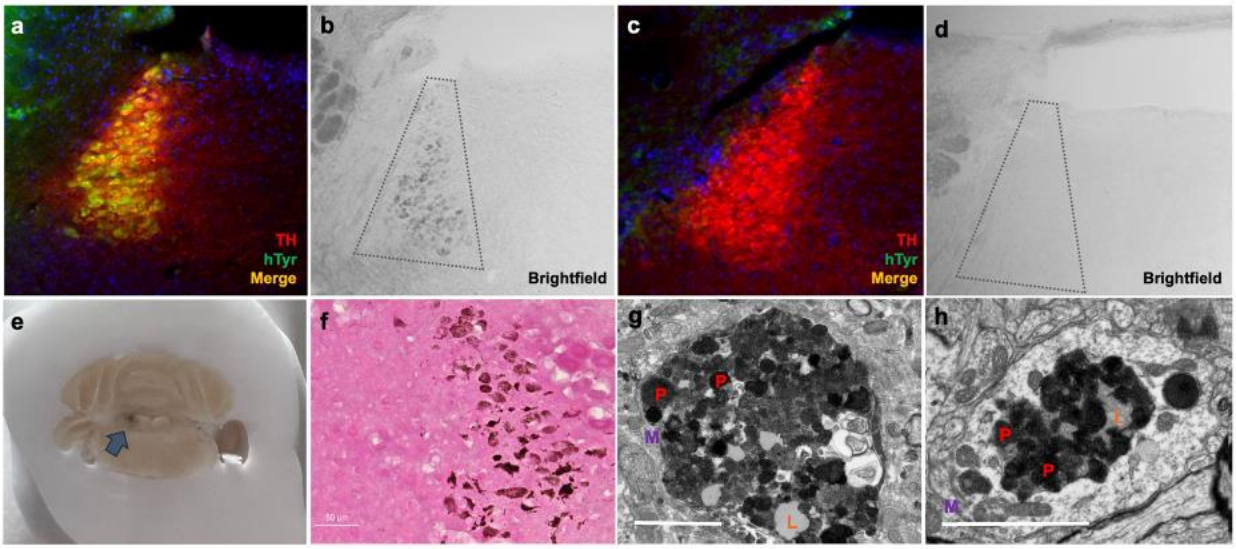

Fig. 1. hTyr induces pigmentation in the LC reminiscent of endogenous NM at 1 week. Mice received stereotaxic injection of AAV5-DIO-hTyr into the LC, driving expression of human tyrosinase in TH-Cre+ experimental animals (**a**) but not in TH-Cre- controls (**c**). Although rodents (TH-Cre- image shown here) do not display endogenous NM (**d**), the expression of hTyr resulted in LC pigmentation visible by brightfield microscopy (**b**) and gross anatomical inspection (arrow) (**e**). This hTyr-derived pigment stained positive for melanin components with Fontana-Masson (**f**), and electron microscopic analysis of these granules (**g**) showed they contain several features characteristic of endogenous NM from aged rhesus macaques (**h**), including pigment of various shades (P, red), lipid droplets (L, orange), and enclosure in a membrane (M, purple). Scale bar = 5 μM. Immunofluorescent and brightfield images (A-D, F) were acquired at 20x magnification.

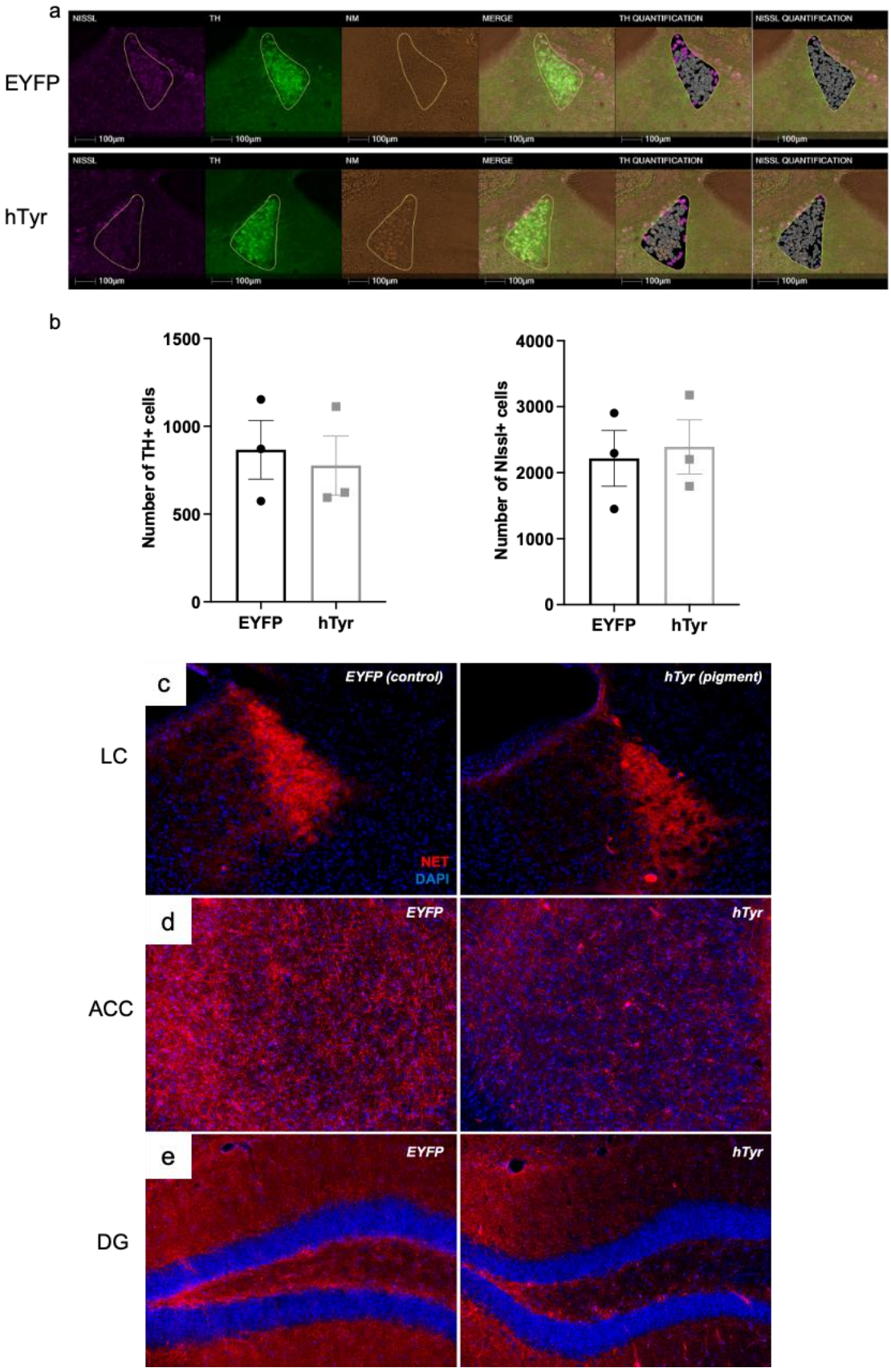

Fig. 2. The presence of NM results in loss of LC fibers but not cell bodies at 1-week. TH-Cre mice received LC infusion of AAV5-DIO-hTyr or EYFP control and were assessed for LC neuron damage 1 week later. hTyr-induced NM expression did not alter LC neuron number (TH+ or Nissl+ cells). Representative immunofluorescent HALO images are shown in (**a)**, quantification (mean ± SEM) shown in (**b**). NM accumulation resulted in substantial loss of axon terminals as measured by NE transporter (NET, red; DAPI, blue) immunoreactivity in the anterior cingulate cortex (ACC) (**c**) and dentate gyrus (DG) (**d**). Images acquired at 20X.

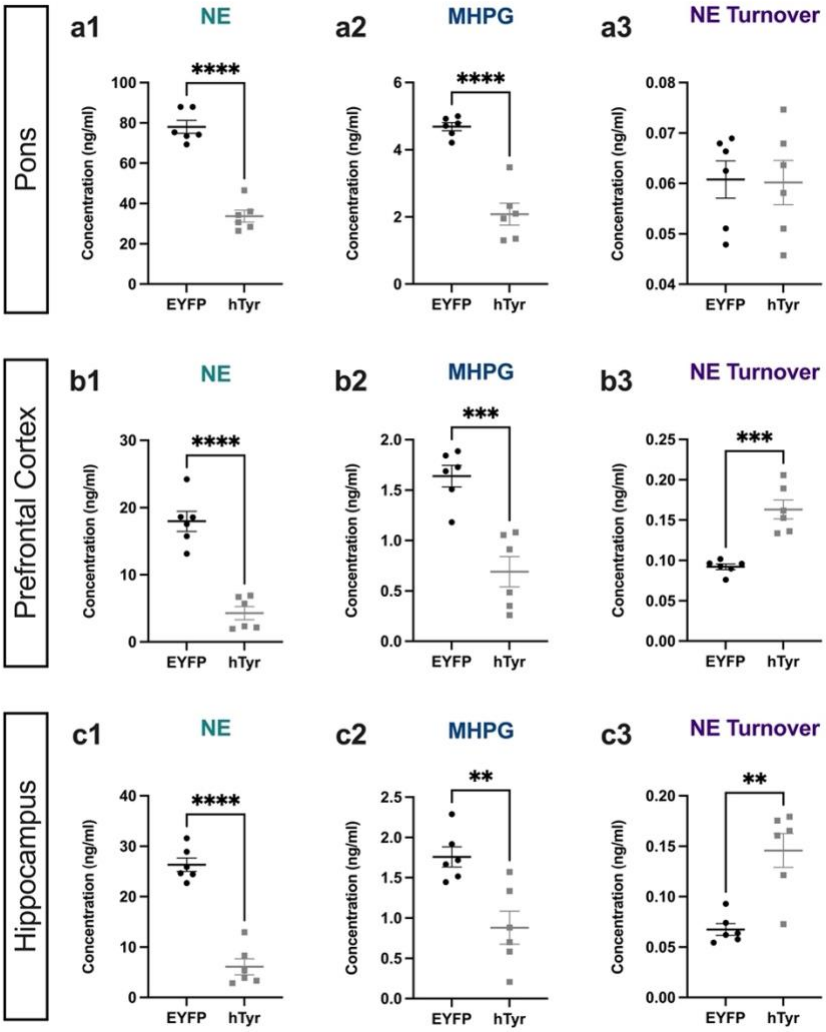

Fig. 3. hTyr-induced NM decreases tissue NE and metabolite levels and increases turnover at 1 week. TH-Cre mice received stereotaxic infusion of AAV-DIO-hTyr or EYFP control into the LC, and tissue monoamine and metabolite levels were measured 1 week later by HPLC in the pons, prefrontal cortex (PFC), and hippocampus. hTyr significantly decreased NE and its primary metabolite MHPG in the pons (**a1-2**), PFC (**b1-2**), and hippocampus (**c1-2**). NE turnover, defined as the MHPG:NE ratio, was increased in PFC (**b3**) and hippocampus (**c3**). Data shown as mean ± SEM. N=6 per group. *p<0.05, **p<0.01, ****p<0.0001.

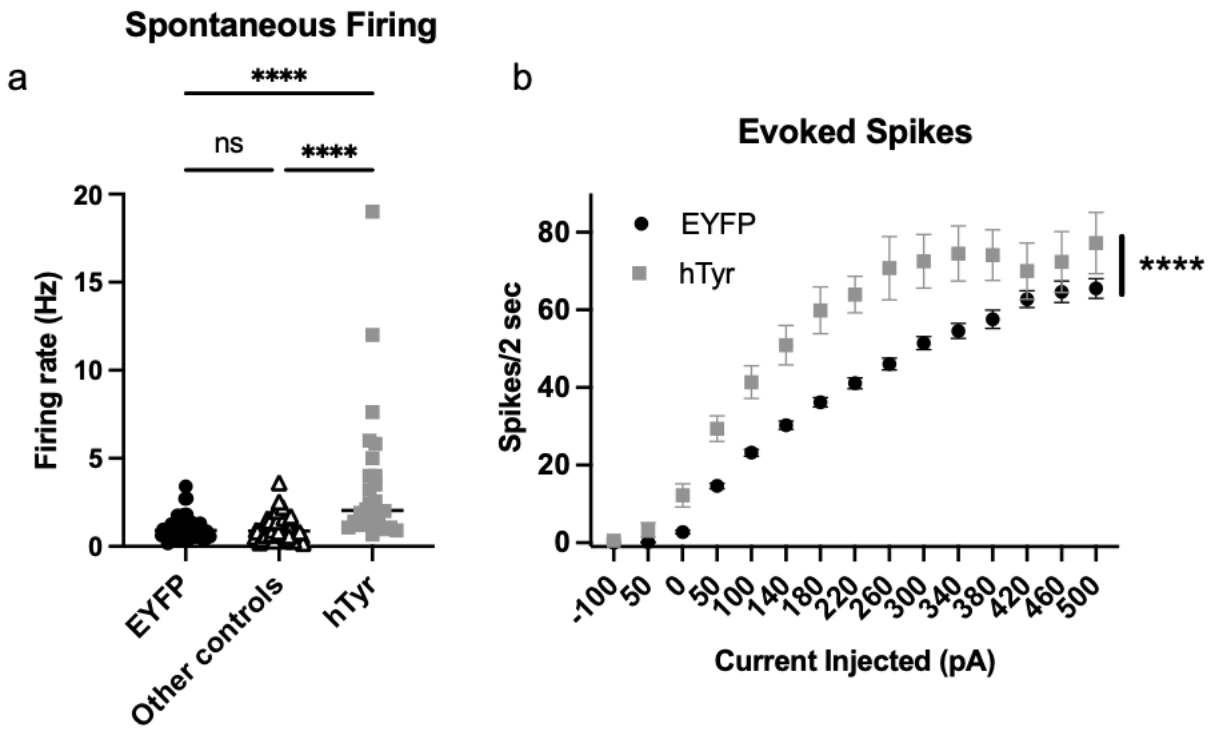

Fig. 4. hTyr-induced NM accumulation causes LC hyperactivity at 1 week. TH-Cre mice received stereotaxic infusion of AAV-DIO-hTyr or EYFP control into the LC, and LC neuron activity was assessed 1 week later by slice electrophysiology. (**a**) NM-containing LC neurons (N=26) had increased spontaneous firing compared to eYFP (N=55) or other controls (N=71; e.g. neighboring LC neurons in the hTyr group that were not expressing NM). (**b**) NM-containing LC neurons (N=24) fired more action potentials following current injection compared to EYFP LC neurons (N=77). ****p<0.0001.

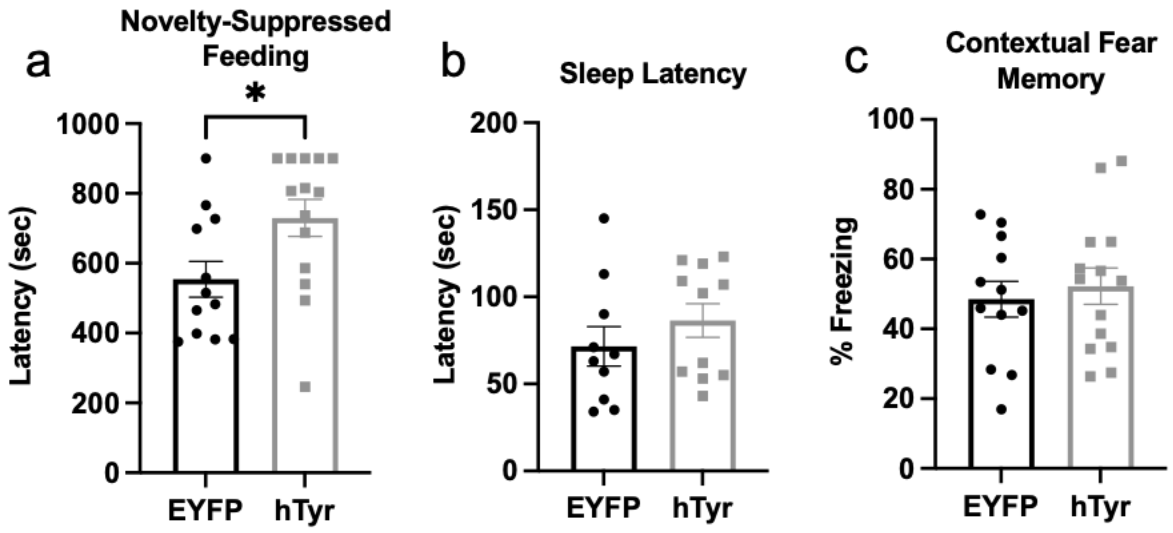

Fig. 5. hTyr-induced NM increases anxiety-like behavior but not arousal or contextual fear memory at 1 week. TH-Cre mice received stereotaxic infusion of AAV-DIO-hTyr or EYFP control into the LC, and behavior was assessed 1 week later. hTyr-expressing mice displayed increased latency to bite the food pellet in the novelty-suppressed feeding test but no difference in latency to sleep in their home cage following gentle handling (**b**) or freezing behavior in the contextual conditioning fear assay (**c**). (N=12-14 per group). *p<0.05.

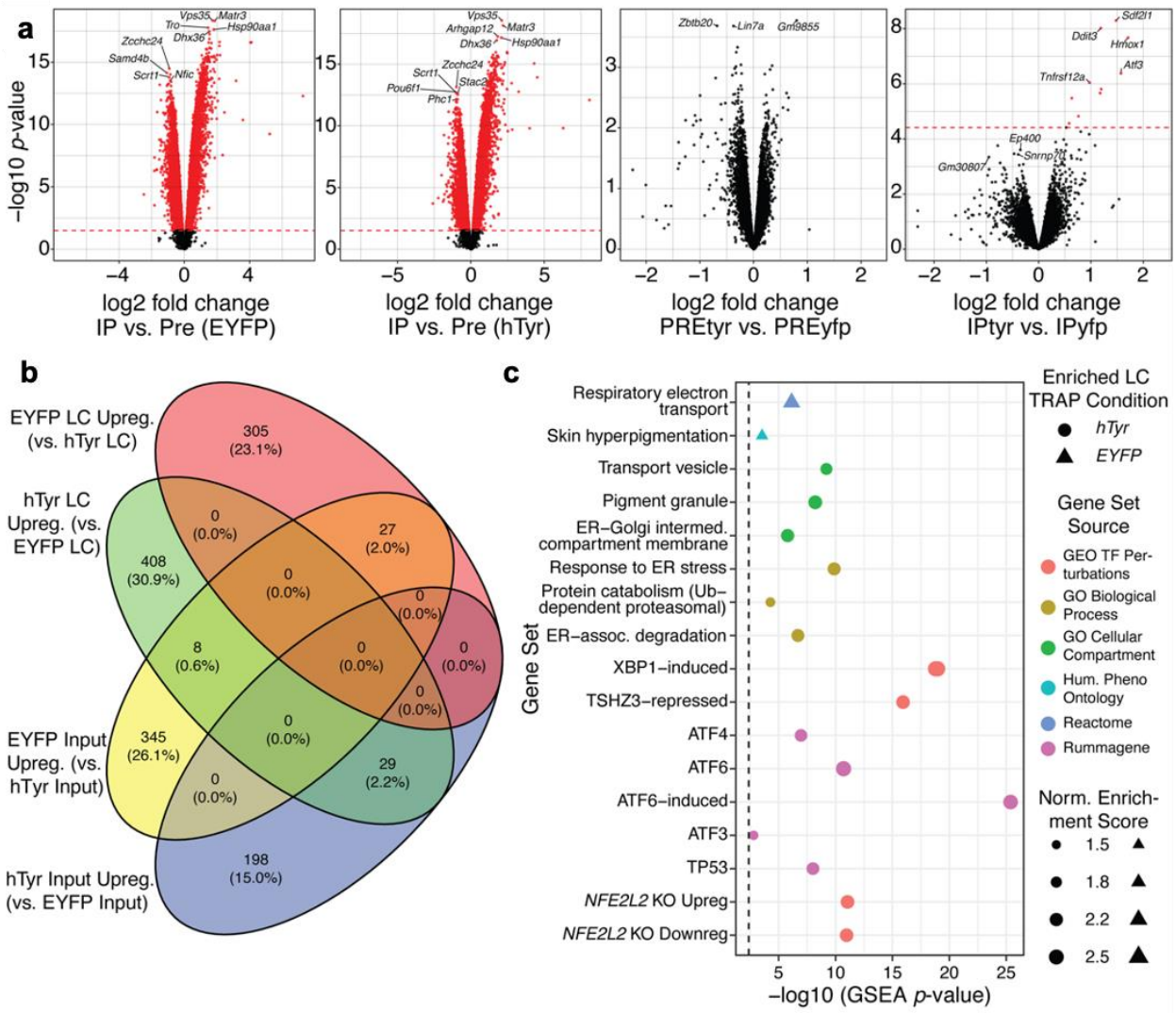

Fig. 6. TRAP-seq at reveals LC-restricted transcriptional responses to NM indicative of endoplasmic reticulum stress at 1 week. TH-Cre+, *Slc6a2-eGFP*/*Rpl10a*+ mice received stereotaxic infusion of AAV-DIO-hTyr or EYFP control into the LC, and transcriptomes were assessed 1 week later by TRAP-seq. (**a**) Volcano plots of differential expression (DE) comparisons from TRAP-seq experiments. Red lines demarcate the FDR threshold (0.05) for considering DE significant. On the left, comparisons between IP (TRAP) and Pre-IP ("input") fractions are shown for mice transduced with EYFP or hTyr, illustrating the magnitude of TRAP enrichment/depletion is similar between the two treatments and that the top-enriched genes (labeled points) are largely

consistent across treatments. On the right are shown comparisons of the Pre-IP or IP across treatments, illustrating that hTyr does not substantially change the surrounding tissue transcriptome relative to EYFP, while specifically inducing a small set of proteostasis genes in the LC. (**b**) Venn diagram comparing the number of genes upregulated at a nominal $p<0.05$ in the EYFP or hTyr condition for each tissue fraction. Note that the vast majority of hTyr-LC upregulated genes are not hTyr-induced in the input sample (29/408 genes), indicating the transcriptional effects of hTyr are LC-specific. (**c**) Select GSEA results from DE analysis between hTyr IP and EYFP IP. The upper half of the plot illustrates ontology and pathway terms, while the lower half illustrates TFs whose target genes are enriched in DE patterns. The size of each point indicates the degree of DE enrichment for the term, the color indicates the source for the term, and the shape of the point indicates whether the term was enriched in EYFP- or hTyr-upregulated genes. As pathways and TF-target sets were tested separately, the more stringent of the two FDR<0.05 thresholds is shown as a dashed vertical line.

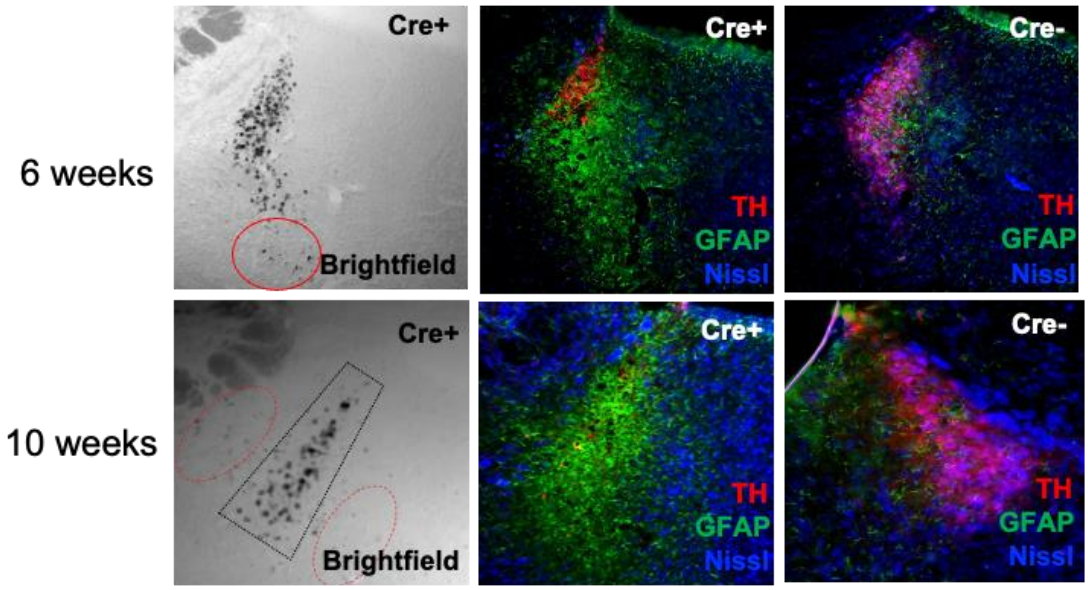

Fig. 7. Prolonged hTyr expression results in NM accumulation and LC degeneration. TH-Cre+ and TH-Cre- mice received stereotaxic infusion of AAV-DIO-hTyr into the LC and aged for 6-10 weeks. Shown are representative images of NM (brightfield), the neuron marker Neurotrace Nissl (blue), the LC marker TH (red), and the astrocyte marker GFAP. Red ovals depict pigment outside the typical confines of the LC. Images were acquired at 20X magnification.

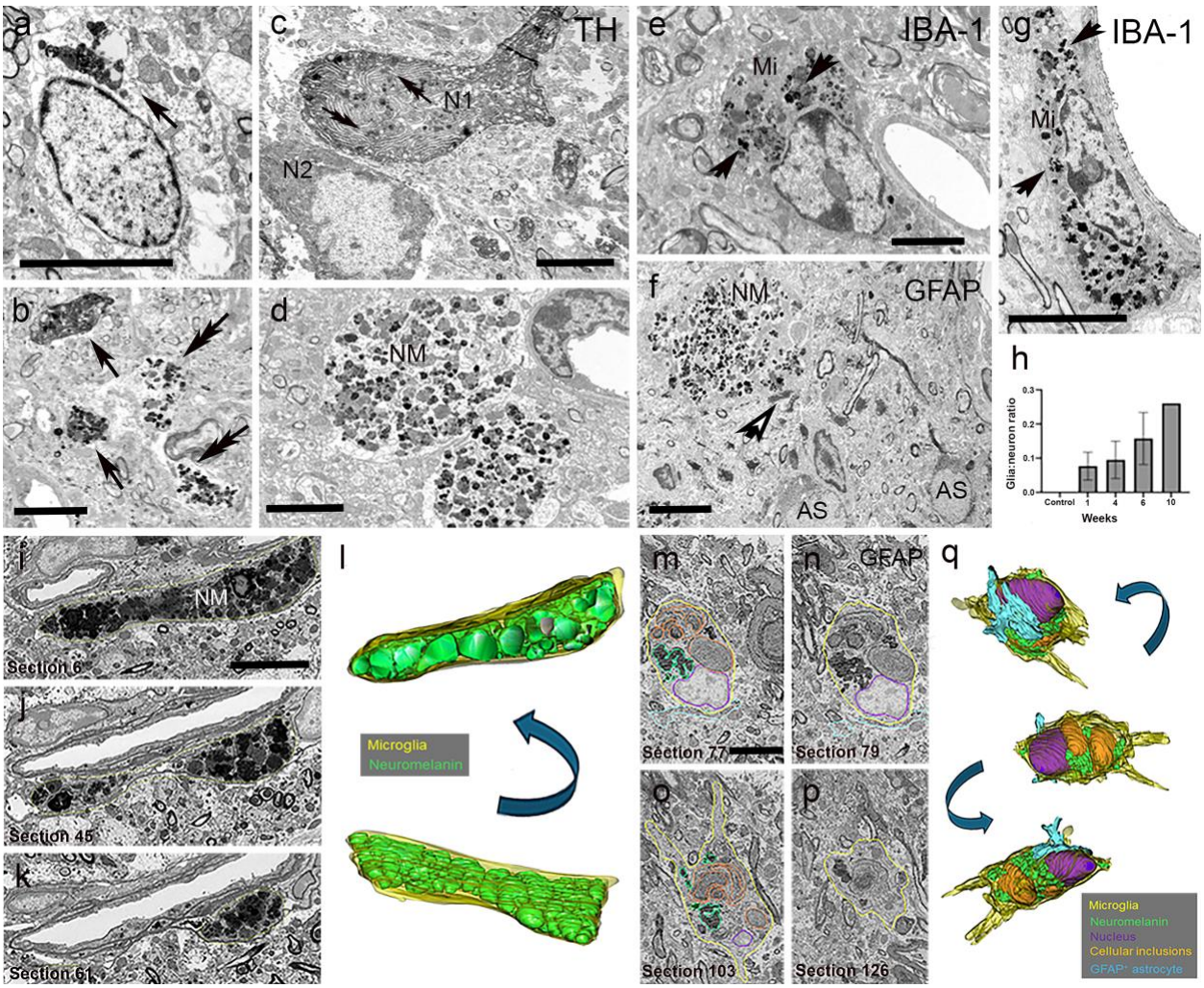

Fig. 8. Transmission 2D EM analysis and 3D ultrastructural reconstruction of neuromelanin (NM) granules in the mouse LC. TH-Cre mice received stereotaxic infusion of AAV-DIO-hTyr or EYFP control into the LC, and electron microscopy was performed 1-10 weeks later. (**a**) Cluster of NM in the cell body of a LC neuron (arrow, 1 week hTyr), (**b, c**) LC tissue (1 week hTyr) immunostained for TH showing NM expression in TH-positive dendritic profiles (arrows in **b**) and a neuronal cell body (N1 in **c**). In **b**, the double arrows indicate NM-containing TH-negative dendrites, while in **c**, they point at intracellular NM granules. Note in **c**, a TH-positive LC neuronal perikaryon (N2) that does not contain NM. (**d**) Large neuropil structures heavily packed with NM granules in the LC (6 weeks hTyr). (**e, g**) Examples of

immunoperoxidase-stained IBA-1-containing microglia (Mi) cell bodies enriched in NM aggregates (arrows) in the LC of a 6 week hTyr mouse. (**f**) GFAP-positive astrocytic profiles (AS) in the close vicinity of a NM-containing neuropil element (6 weeks hTyr). Note the lack of NM in AS cell bodies, and the close apposition between an AS process (open arrow in **f**) and the NM-containing element. (**h**) The ratio of NM-containing glia:neuron profiles in the LC of control (no hTyr: n=3) and experimental (hTyr 1 week: n=3; 4 weeks: n=2; 6 weeks: n=4; 10 weeks: n=1) mice. (**i-k, m-p**) Serial ultrastructural images of NM clusters (**i-k**) and a putative microglia cell body profile **(m-p)** from the LC of a 6 week hTyr mouse used in *Reconstruct* (NIH) to create their respective 3D models (**l, q**). Different rotated images of the 3D reconstructed models showing the NM clusters (**l**) and the intracellular distribution of NM, cytoplasm inclusions of degenerated axonal profiles and nucleus in the microglia (**q**). The tissue used for the 3D analysis of the microglia was immunostained with GFAP and allowed for the analysis of the spatial interaction between the microglia and GFAP-positive astrocytic processes. A total of 83 and 139 serial images, respectively, were used in the 3D reconstruction of the NM clusters (**l**) and the microglia (**q**). Scale bars in **a-g, i** (**applies to j, k**) **and m** (**applies to n-p**) = 5µm.

Abbreviations: Mi=Microglia; NM=Neuromelanin; N=Neuron; AS=Astrocyte. Scale bar value: A: 5 mm; B,C,F: 2 mm; D,E,G: 3 mm.

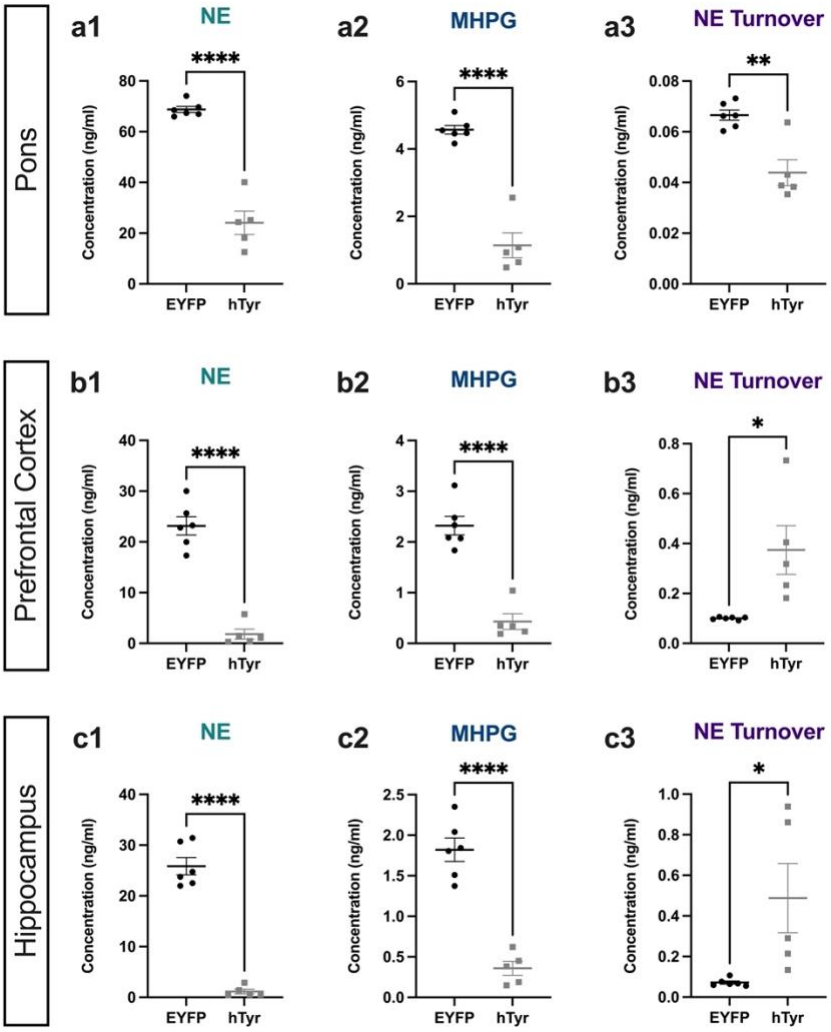

Fig. 9. hTyr-induced NM accumulation depletes tissue NE and metabolite levels and dysregulates turnover at 6 weeks. TH-Cre mice received stereotaxic infusion of AAV5-DIO-hTyr or EYFP control into the LC, and tissue monoamine and metabolite levels were measured 6 weeks later by HPLC in the pons, prefrontal cortex (PFC), and hippocampus. hTyr significantly and robustly decreased NE and metabolite MHPG in the pons (**a1-2**), PFC (**b1-2**), and hippocampus (**c1-2**). NE turnover (MHPG:NE ratio) was decreased in the pons (**a3**), but decreased in the PFC (**b3**) and hippocampus (**c3**). Data shown as mean ± SEM. N=8 per group. *p<0.05, **p<0.01, ****p<0.0001.

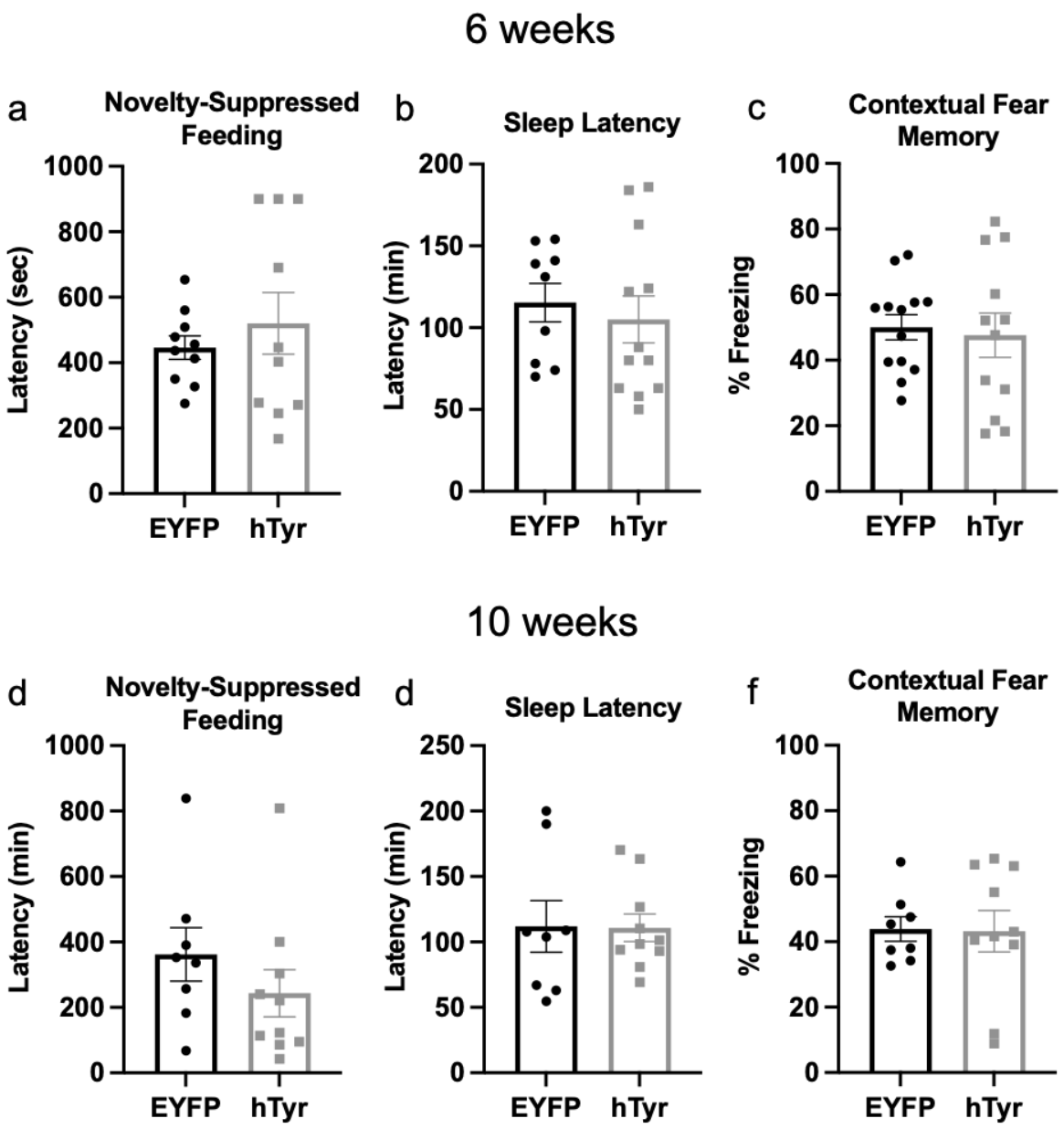

Fig. 10. NM accumulation and subsequent neurodegeneration has no effect on behavior. TH-Cre mice received stereotaxic infusion of AAV5-DIO-hTyr or EYFP control into the LC, and behavior was assessed 6 (**a-c**) or 10 weeks (**d-f**) later. hTyr-expressing mice displayed no difference in latency to eat in the novelty-suppressed feeding test (**a,d**), sleep latency (**b,e**), or freezing in response to shock-associated context (**c,f**) at either time point. (N=8-13 per group).

Table 1. IHC antibodies

Antibodies	Host	Manufacturer	Catalog #	Dilution
Tyrosine hydroxylase	Chicken	Abcam	ab76442	1:1000
Norepinephrine transporter	Mouse	Mab Technologies	NET05-2	1:1000
Human tyrosinase	Mouse	Thermo Fisher Scientific	MS-800-B1	1:500
GFAP	Guinea Pig	Synaptic Systems	173 004	1:1000
NeuroTrace 435/455 Blue Fluorescent Nissl Stain	NA	Thermo Fisher Scientific	N21479	1:500
Alexa Fluor 488 Anti-Rabbit	Goat	Thermo Fisher Scientific	A-11008	1:500
Alexa Fluor 488 Anti-Guinea Pig	Goat	Thermo Fisher Scientific	A-11073	1:500
Alexa Fluor 568 Anti-Chicken	Goat	Thermo Fisher Scientific	A-11041	1:500

Table 2. Monoamine levels measured by HPLC. Data shown as mean ± SEM. N=5-6 per group.

A) 1-week post-infusion

	Pons		PFC		Hippocampus	
	EYFP	**hTyr**	**EYFP**	**hTyr**	**EYFP**	**hTyr**
DA	11.37 ± 0.69	10.39 ± 0.91	20.14 ± 8.32	4.54 ± 0.38	3.53 ± 1.29	2.33 ± 0.28
DOPAC	6.98 ± 0.49	7.53 ± 0.72	3.08 ± 0.61	2.40 ± 0.20	2.52 ± 0.26	2.47 ± 0.45
DOPAC:DA	0.62 ± 0.03	0.72 ± 0.02	0.30 ± 0.08	0.53 ± 0.02	1.04 ± 0.20	1.11 ± 0.19
5-HT	170.9 ± 3.38	162.5 ± 4.33	40.66 ± 3.34	45.30 ± 2.94	69.17 ± 3.43	63.04 ± 3.73
5-HIAA	58.31 ± 3.09	61.95 ± 4.11	7.72 ± 0.22	8.59 ± 0.45	7.72 ± 0.22	8.59 ± 0.45
5-HIAA:5-HT	0.34 ± 0.02	0.38 ± 0.20	0.20 ± 0.02	0.19 ± 0.01	0.36 ± 0.03	0.38 ± 0.01

B) 6-weeks post-infusion

	Pons		PFC		Hippocampus	
	EYFP	**hTyr**	**EYFP**	**hTyr**	**EYFP**	**hTyr**
DA	9.14 ± 0.90	7.33 ± 1.06	43.34 ± 22.50	30.36 ± 16.71	2.54 ± 0.61	1.99 ± 0.37
DOPAC	6.34 ± 0.49	5.39 ± 0.70	6.33 ± 1.99	5.22 ± 1.31	1.75 ± 0.18	2.74 ± 0.28
DOPAC:DA	0.71 ± 0.05	0.75 ± 0.08	0.30 ± 0.06	0.28 ± 0.07	0.84 ± 0.16	1.53 ± 0.22
5-HT	162.6 ± 6.20	146.7 ± 4.90	62.40 ± 5.61	57.03 ± 3.27	71.83 ± 3.84	71.54 ± 3.64
5-HIAA	71.80 ± 5.58	50.41 ± 1.68	13.65 ± 2.19	10.02 ± 0.27	31.89 ± 2.02	23.78 ± 0.78
5-HIAA:5-HT	0.44 ± 0.02	0.35 ± 0.02	0.21 ± 0.01	0.18 ± 0.01	0.45 ± 0.02	0.34 ± 0.03